Mechanical degradation of Longmaxi shale exposed to water-based fluids and supercritical carbon dioxide

Jianting Du, Andrew J Whittle, Liming Hu, Thibaut Divoux, Jay N Meegoda

To cite this version:

Jianting Du, Andrew J Whittle, Liming Hu, Thibaut Divoux, Jay N Meegoda. Mechanical degradation of Longmaxi shale exposed to water-based fluids and supercritical carbon dioxide. Journal of Rock Mechanics and Geotechnical Engineering, 2024, ⟨10.1016/j.jrmge.2024.08.009⟩. ⟨hal-04907427⟩

HAL Id: hal-04907427

https://hal.science/hal-04907427v1

Submitted on 23 Jan 2025

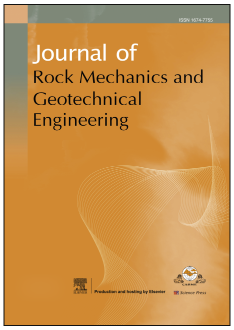

Mechanical degradation of Longmaxi shale exposed to water-based fluids and supercritical carbon dioxide

Jianting Du, Andrew J. Whittle, Liming Hu, Thibaut Divoux, Jay N. Meegoda

PII: S1674-7755(24)00359-7

DOI: https://doi.org/10.1016/j.jrmge.2024.08.009

Reference: JRMGE 1678

To appear in: *Journal of Rock Mechanics and Geotechnical Engineering*

Received Date: 25 February 2024

Revised Date: 9 July 2024

Accepted Date: 14 August 2024

Please cite this article as: Du J, Whittle AJ, Hu L, Divoux T, Meegoda JN, Mechanical degradation of Longmaxi shale exposed to water-based fluids and supercritical carbon dioxide, *Journal of Rock Mechanics and Geotechnical Engineering*, https://doi.org/10.1016/j.jrmge.2024.08.009.

Full length article

Mechanical degradation of Longmaxi shale exposed to water-based fluids and supercritical carbon dioxide

Jianting Du [a, *], Andrew J. Whittle [b], Liming Hu [c], Thibaut Divoux [d, e], Jay N. Meegoda [c, f]

[a] State Key Laboratory of Internet of Things for Smart City and Department of Civil and Environmental Engineering, University of Macau, Macau, China

[b] Department of Civil and Environmental Engineering, Massachusetts Institute of Technology, Cambridge, MA 02139, USA

[c] State Key Laboratory of Hydro-Science and Engineering, Tsinghua University, Beijing, 100084, China

[d] MultiScale Material Science for Energy and Environment, UMI 3466, CNRS-MIT, Cambridge, MA 02139, USA

[e] ENSL, CNRS, Laboratoire de Physique, F-69342 Lyon, France

[f] Department of Civil and Environmental Engineering, New Jersey Institute of Technology, Newark, NJ 07102, USA

* Corresponding author. E-mail: jiantingdu@um.edu.mo (Jianting Du).

Abstract: Mechanical alterations in shale formations due to exposure to water-based fracturing fluids and supercritical carbon dioxide ($ScCO_2$) significantly affect the performance of shale gas exploration and CO_2 geo-sequestration. In this study, a hydrothermal (HT) reaction system was set up to treat Longmaxi shale samples of varying mineralogies (carbonate-, clay-, and quartz-rich) with different fluids, i.e. deionized (DI) water, 2% potassium chloride (KCl) solution, and $ScCO_2$ under HT conditions expected in shale formation. Statistical micro-indentation was conducted to characterize the mechanical property alterations caused by the shale-fluid interactions. An in situ morphological and mineralogical identification technique that combines scanning electron microscopy (SEM) and backscattered electron (BSE) imaging with energy-dispersive X-ray spectroscopy (EDS) was used to analyze the microstructural and mineralogical changes of the treated shale samples. Results show no apparent changes in the Young's modulus, E, and hardness, H, after treatment with DI water under room temperature (20 °C) and atmospheric pressure for 7 d. In contrast, E and H were decreased by 31.2% and 37.5% at elevated temperature (80 °C) and pressure (8 MPa), respectively. The addition of 2% KCl into DI water mitigated degradation of the mechanical properties. Quartz-rich shale specimens are the least sensitive to the water-based fracturing fluids, followed by the clay-rich and carbonate-rich shale formations. Based on in situ morphological and mineralogical identification, the primary factors for the mechanical degradation induced by water-based fluids include carbonate dissolution, clay swelling, and pyrite oxidation. Slight increases in the measured E and H and compression of porous clay aggregates were observed after treatment with $ScCO_2$. The major factor contributing to the mechanical changes resulting from the exposure to $scCO_2$ appears to be the competition between swelling caused by adsorption and compression of shale matrix.

Keywords: Shale gas; Carbon dioxide geo-sequestration; Grid micro-indentation; Hydrothermal treatment; Morphological and mineralogical identification

1. Introduction

Shale formations have significant roles in industrial applications, including CO_2 geological sequestration (Nguyen et al., 2016; Sun et al., 2016) and natural gas production (Ju et al., 2014; Jiang et al., 2022; He et al., 2023). Due to the low permeability of shale formations (Katende et al., 2023a), water-based hydraulic fracturing fluids are extensively utilized to create extensive networks of fractures (Peirce and Bunger, 2015; Asahina et al., 2018; Taghichian et al., 2018; Yin et al., 2020; Zhang et al., 2023). Mechanical properties of shale, such as elastic stiffness (Wang et al., 2021), creep (Chen et al., 2009; Benge et al., 2023), and fracture toughness (Akono et al., 2012; Akono and Kabir, 2016), are critical for fracture generation and propagation, and consequently impact the shale gas exploration. In the context of geological sequestration, CO_2 is injected into shale formations in a supercritical state due to the elevated pressure and temperature conditions within the shale formations (Zhang et al., 2020). Mechanical alterations induced by the interactions between shale and water-based fluids and $ScCO_2$ impact the performance of production and injection systems, including the rate of gas recovery (Wang et al., 2024), proppant embedment (Corapcioglu et al., 2014; Katende et al., 2021; Katende et al., 2023b), wellbore stability (Wu et al., 2015b), and reservoir subsidence (Zhang et al., 2013). Thus, it is essential to assess the resulting mechanical alterations of shale formations and reveal the underlying mechanism.

The mechanical properties of shale are typically determined through macroscopic experiments (Guo et al., 2012; Gao et al., 2015) that measure stress-strain properties on reduced core samples (i.e. specimens prepared by drilling and grinding to centimeter scale). However, these conventional macroscopic measurements have several limitations. For instance, these relatively large specimens often exhibit high inter-sample variability due to flaws within the cores. Moreover, due to the unstable structure and physicochemical properties of shale, obtaining complete cores from horizontal wells of the wellbore is rather challenging (Wang et al., 2012; Ma and Chen, 2014).

Over the past decades, advances in indentation methods, initially introduced by Oliver and Pharr (1992) and further elaborated in their subsequent works (Oliver and Pharr, 2004), have enabled the acquisition of local mechanical properties for composite materials at micro- and nano-scale. Shales, which belong to the category of fine-grained sedimentary rocks, primarily consist of granular minerals such as quartz, feldspar, carbonates, and pyrite, in addition to densely packed aggregates of clay particles and organic matter. As shown in Fig. 1, the structure of shale can be considered at five levels, from the individual clay platelets to the scale of macroscopic shale (Du et al., 2022). Level IV is the scale of conventional macroscopic laboratory experiments that assume shale to be mechanically homogeneous (Colmenares and Zoback, 2002; Pan et al., 2020). Shale can be considered a composite material at the mesoscale (i.e. Level III), representing the elementary shale block (Bobko et al., 2011; Du et al., 2021). The representative shale block can be further broken down into the constituent mineral phases at Levels I and II. Level 0 is the scale of the clay sheet (0.7 nm and 1.0 nm in thickness for the 1:1 and 2:1 phyllosilicate clay minerals, respectively (Zhang et al., 2010)). The properties of clay sheet are typically studied using molecular simulation (Ebrahimi et al., 2012). The mesoscale (Level III, Fig. 1) corresponds to a matrix-inclusion composite (with submillimeter length scale), comprising a porous clay/organic composite intermixed with hard/soft inclusions (e.g. calcite, quartz, and pyrite), and consequently can be regarded as the fundamental building unit of shale (Du et al., 2022). As such, the mechanical properties measured at mesoscale can be representative of the properties of bulk shales. The upscaling/homogenization of the fundamental building unit of shale has been studied to predict the macroscopic elastic properties (Ortega et al., 2007; Bobko and Ulm, 2008; Goodarzi et al., 2016; Charlton et al., 2021; Graham et al., 2022). However, direct assessment of the mechanical property alterations for bulk shale through a mesoscale experimental analysis is still limited. Recent experimental studies (Du et al., 2021) determined the characteristic indentation depth beyond which shale properties are homogeneous, regardless of the spatial distribution of constituent mineral phases. This finding enables the use of micro-indentation tests for evaluating the mechanical degradation of bulk shale induced by the shale-fluid interactions and, in turn, mitigates the need for expensive and time-consuming conventional experiments.

To date, the mechanical property alterations caused by shale-ScCO$_2$-water interaction have been widely studied (Akono et al., 2019; Manjunath et al., 2023). The acidic environment formed by the reaction between water and ScCO$_2$ has been considered the primary factor of the mechanical degradation of shale (He et al., 2011; Wang et al., 2016; Fuchs et al., 2019; Chen et al., 2021). However, previous studies have rarely studied the mechanical alterations induced solely by ScCO$_2$. While mechanical degradations in clay-rich shale formations have attracted most research focus due to the abundance of 'problematic' clay minerals that exhibit crystalline/osmotic swelling, such as smectites (Lutz, 1935; Norrish, 1954; Chenevert, 1970; Wong, 1998; Wu et al., 2015a; Wu et al., 2015b), relevant studies for formations that are rich in carbonate or quartz minerals are limited. In addition, the roles of other constituent minerals, such as quartz, carbonate, and pyrite, in the induced mechanical alterations remain unclear.

In this paper, we investigated alterations in the mechanical properties of Longmaxi shale after being treated with different fluids (i.e. DI water, 2% KCl brine, and ScCO$_2$) for 7 d. The actual temperature and pressure conditions of the Longmaxi shale formation are mimicked using a hydrothermal (HT) reaction system. Statistical micro-indentation is conducted to characterize the changes in mechanical properties associated with these shale-fluid interactions. We also developed an in situ morphological and mineralogical identification technique to uncover the underlying mechanism. The concept of this study lies in using a mesoscale analysis to evaluate changes in mechanical properties for applications in hydraulic fracturing and CO$_2$ sequestration.

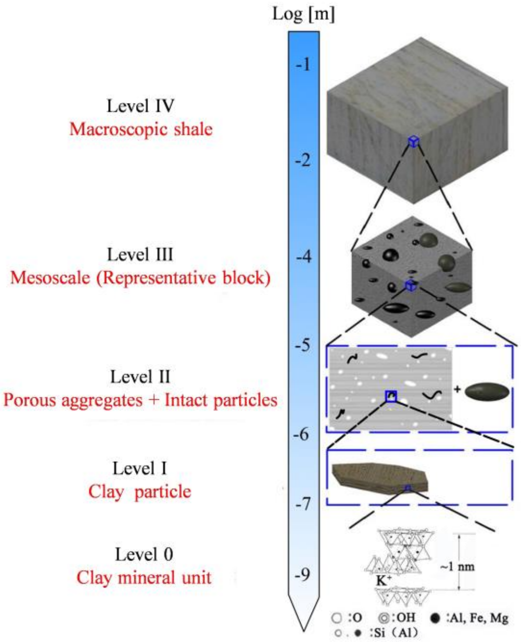

Fig. 1. Multiscale conceptual model of shale structure (Du et al., 2023).

2. Materials and methods

2.1. Rock samples and surface preparation

The Longmaxi shale formation located in China's Sichuan Basin has emerged as a primary target for exploration and development of shale gas due to its abundance of total organic content (0.35% - 18.4%) and high vitrinite reflectance (R_o = 1.8% - 4.2%) (Dai et al., 2014). Three Longmaxi shale samples with distinct mineralogy are used in this study. None of these shale samples have visible bedding planes. The mineralogy of the studied shale samples is first assessed by X-ray diffraction (XRD) (Choobbasti and Kutanaei, 2017; Yu et al., 2022). The diffraction pattern was further qualitatively and quantitatively analyzed using the Rietveld refinement method (Qin et al., 2023; Sun et al., 2024). The three samples were incinerated at 440 °C for 12 h using a Thermo Scientific incinerator to measure the organic matter content. The quantitative mineralogy and organic matter content results are presented in **Table 1**. Samples #1, #2, and #3 are carbonate-rich (calcite and dolomite, ~41%), clay-rich (illite and chlorite, ~45%), and quartz-rich (quartz, ~42%), respectively.

Table 1

Quantitative mineralogy and organic matter content for the three Longmaxi shale samples used in this study.

Components	Mass fraction (%)		
	Sample #1	Sample #2	Sample #3
Albite (A)	-	11	16.1
Calcite (C)	18.4	2.3	3.4
Chlorite (Ch)	-	9.9	-
Dolomite (D)	22.3	1.6	-
Illite (I)	26.8	34.9	29.2
Pyrite (P)	3	2	7
Quartz (Q)	23.2	36.2	41.5
Organic matter	6.3	2.1	2.8

Small cuboidal specimens with dimensions of 2 cm × 2 cm × 1 cm (width × length × thickness) were carefully polished using a sequence of 6 Silicon Carbide papers with increasing grit size (up to 0.25 μm). The surface roughness was evaluated through a root-mean-squared (RMS) average of the surface topography, which was measured by the Atomic Force Microscope (AFM) technique (Simpson et al., 1999). Similar RMS roughness was obtained for carbonate-rich, clay-rich, and quartz-rich shale samples, which were 16 nm, 38 nm, and 25 nm, respectively. AFM characterization of the polished surface of the carbonate-rich sample shows RMS roughness, i.e. R_q = 16 nm (Fig. 2).

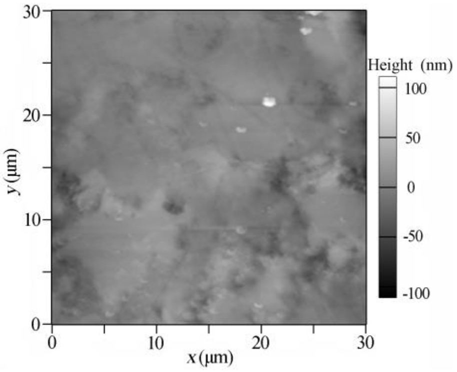

Fig. 2. Representative AFM map of a region of interest prepared by mechanical polishing.

2.2. Statistical micro-indentation test

To reduce measurement errors caused by rock surface preparation and its heterogeneity, grid micro-indentation or statistical micro-indentation, which performs the indentation tests on sample surface with uniform distribution of spaced square lattice, was employed to characterize the linear and nonlinear mechanical responses of the shale samples at sub-micrometer length scales. Indentation tests were conducted using a Microtest indenter (Anton Paar, Graz, Austria). The Microtest platform can apply loads ranging from 0.03 N to 30 N with a resolution of 0.3 mN. The indentation depth can be measured up to 200 μm with a resolution of 0.3 nm. The obtained massive indentation data were then analyzed assuming a Gaussian distribution (mean μ and standard deviation σ). The data collection process follows a prescribed load function, illustrated in Fig. 3a. The load was incrementally increased at a constant rate until reaching a maximum force, and then it was maintained for 180 s during the holding phase to account for sample creep. Subsequently, the force was unloaded at the same constant rate as the loading phase. The indentation tests were conducted on a 15 × 15 grid with a uniform separation of 300 μm to prevent interactions between adjacent indents (Luo et al., 2020). As the indentation depth significantly exceeds the characteristic size of the constituent phases in the heterogeneous material, the observed indentation response represents the spatially averaged behavior of the material (Luo et al., 2021). Previous research conducted by Du et al. (2021) demonstrated that the mechanical response of Longmaxi shale becomes homogeneous and independent of its complex heterogeneous microstructure when the indentation depth reaches a critical range of 8 - 10 μm, indicating that the mechanical properties of the bulk shale can be evaluated at this length scale.

In previous work (Du et al., 2021), such a characteristic indentation depth was used in grid indentation measurements on carbonate-rich, clay-rich, and quartz-rich Longmaxi shale samples to determine the homogenous mechanical properties of the three shale samples. Moreover, similar homogenization depths (i.e. >5 μm) have been reported independently for Longmaxi shale samples by Luo et al. (2021). Therefore, by adjusting the maximum indentation load, a target indentation depth of 8 - 10 μm was used in this study to assess the homogenous mechanical properties of the three Longmaxi shale samples. It is noted that the experimental facility and the shale samples used in this study were the same as that used in Du et al. (2021).

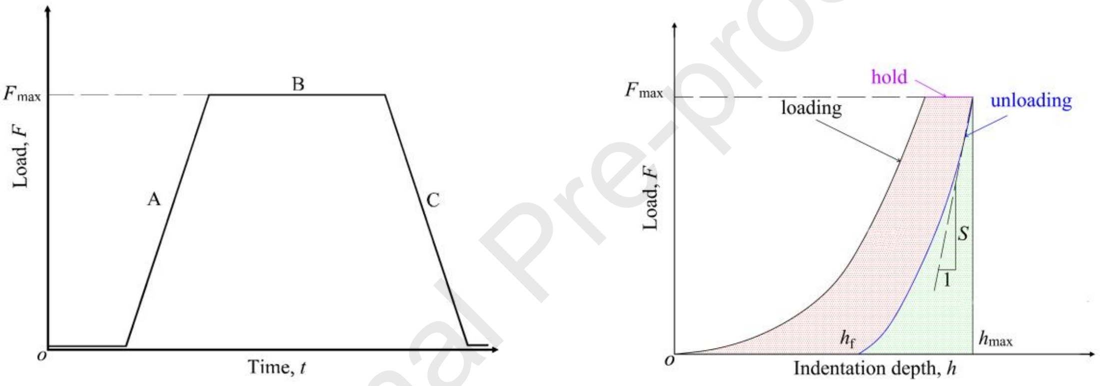

(a) (b)

Fig. 3. Prescribed indentation loading function (a) and typical load vs. depth response (b). The loading, holding, and unloading sections are denoted as segments A, B, and C, respectively. Key measurements obtained from the load versus depth curve include the initial unloading slope, S, maximum depth, h_{max}, residual depth, h_f, and the maximum force, F_{max}.

The indentation hardness can be obtained by

$$H = \frac{F_{max}}{A_c} \quad (1)$$

where A_c is the well-defined contact area function for a Berkovich tip.

The Young's modulus can then be determined from the load versus depth curve during the unloading phase as follows:

$$E = (1 - \nu^2) \bigg/ \left(\frac{1}{M} - \frac{1 - \nu_i^2}{E_i} \right) \quad (2)$$

where ν_i and ν are the Poisson's ratio of the diamond indenter (ν_i = 0.07) and the test sample, respectively; E_i is the Young's modulus of the diamond indenter (E_i =1140 GPa); M is the indentation modulus of the sample, which can be obtained as follows:

$$\frac{S}{M\sqrt{A_c}} = \frac{2}{\sqrt{\pi}} \quad (3)$$

The contact stiffness, S, can be determined by differentiating the load vs. depth curve (unloading phase) at the maximum load (see Fig. 3b):

$$S = \frac{\delta F}{\delta h}\Big|_{h_{max}} \quad (4)$$

2.3. In situ morphological and mineralogical identification

An in situ morphological and mineralogical identification technique is developed based on SEM/BSE-EDS analysis. A Carl Zeiss Merlin HR-

SEM system (ZEISS AG, Jena, Germany) was used to perform electron microscopy imaging and EDS mapping. This system also facilitated in situ mineralogical identification through EDS analysis provided by the equipped electron backscatter diffraction (EBSD) analyzers. The SEM/BSE imaging was performed with an accelerating voltage of 15 kV, and a working distance of 10 mm. All the SEM/BSE images were taken with a pixel resolution of 800 × 1024. The procedures of surface morphology characterization and mineral identification are illustrated in Fig. 4:

(1) A fixed region-of-interest (ROI) through SEM imaging is used before and after fluid treatments to accurately characterize the alterations in surface morphology.
(2) The EBSD analyzers are incorporated to generate high-resolution BSE images and EDS maps with a pixel resolution of 800 × 1024.
(3) Using Matlab coding, the quantitative element information stored in each pixel (representing real dimensions of 0.3 μm × 0.3 μm) is extracted. The in situ mineralogy is identified pixel by pixel based on the XRD results and the distinctive chemical composition of each phase present in the Longmaxi shale samples.
(4) The physical and mineralogical properties, such as the microstructure, spatial distribution, and area fraction of each constituent phase are derived from the 'digital mineral map'.

Fig. 5 shows the representative mineral maps of the three Longmaxi shales. The area fraction of carbonate minerals was estimated at 40% (20.2% calcite and 18.7% dolomite) for sample #1 (carbonate-rich). The clay minerals, i.e. illite and chlorite, were identified with an area fraction of 49% in sample #2 (clay-rich). Sample #3 (quartz-rich) exhibited a 45% area fraction of quartz. The size of the area for the mineralogical identification was selected following two constraints. On one hand, the scanned area should be large enough to cover the representative elementary area of the bulk shale. On the other hand, the scanned area should be small enough to ensure the size of each pixel in the EDS maps, which is controlled by the scanning resolution (800 × 1024 pixels in this study), will not exceed the typical particle size of each constituent mineral. Otherwise, a mixture of constituent mineral phases will be included in most of the individual pixels. In this study, with a scanned area of 240 μm × 300 μm, each pixel corresponds to a real size of 300 nm × 300 nm, ensuring that the content of mixtures identified in each area was typically less than 5%. The quantitative mineralogy of the three samples measured by the in situ mineralogical identification was then compared with the results obtained from the XRD analysis. It is noted that using the XRD analysis and in situ mineralogical identification, a direct comparison of the results obtained from the two methods is reasonable because the key different minerals have similar specific gravity, typically within a range of 2.65-2.82 (Abedi et al., 2016). It is shown that the fraction of all the principal mineral phases contained in the three samples exhibits a good agreement with each other. Furthermore, a total of 8 regions of interest were then tested on sample #1, to verify whether the scale of the testing area is sufficient to provide a representative elementary area of the bulk shale. Results show that the measured area fraction of each mineral phase ranges with a small standard deviation (0.5% - 5%). This indicates that at the measurement scale of 240 μm × 300 μm, the in situ micro-scale identification method can avoid the effect of heterogeneous nature of shale material on the mineralogy, and can obtain the quantitative mineralogy of bulk shale. Compared to the organic content, the in situ identification obtained lower values than those obtained from the incineration method. Organic matter is typically identified to be mixed with other minerals such as the O&CL (mixture of organic and clay) and O&Q (mixture of organic and quartz), as shown in Fig. 5a. This may be because the organic matter is most stored in the nano/meso-scale pores in the shale samples (Kuang et al., 2022) and the scanning resolution of the in situ identification is insufficient to detect all the organic content contained.

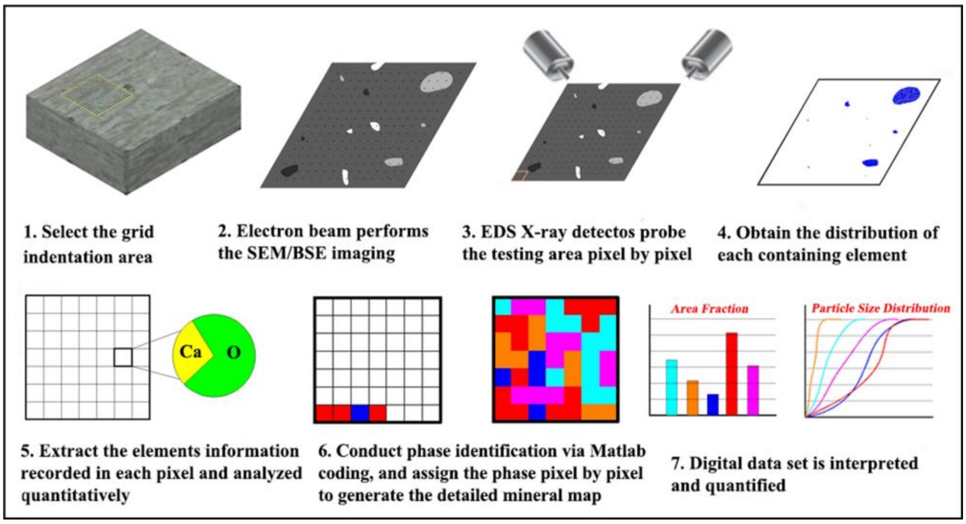

Fig. 4. Procedures for in situ morphological and mineralogical identification.

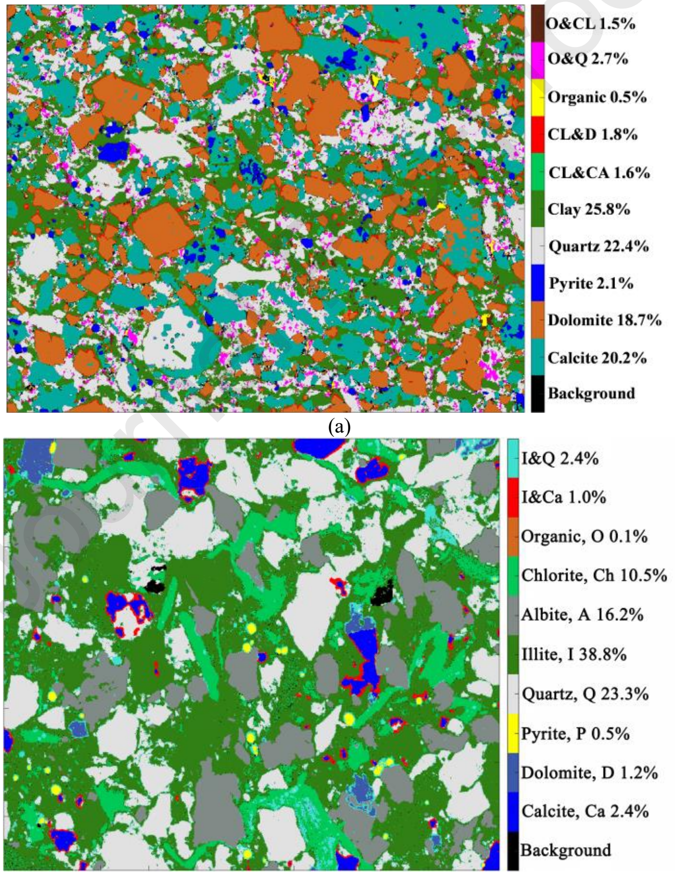
O&CL 1.5%
O&Q 2.7%
Organic 0.5%
CL&D 1.8%
CL&CA 1.6%
Clay 25.8%
Quartz 22.4%
Pyrite 2.1%
Dolomite 18.7%
Calcite 20.2%
Background
I&Q 2.4%
I&Ca 1.0%
Organic, O 0.1%
Chlorite, Ch 10.5%
Albite, A 16.2%
Illite, I 38.8%
Quartz, Q 23.3%
Pyrite, P 0.5%
Dolomite, D 1.2%
Calcite, Ca 2.4%
Background

(a)

(b)

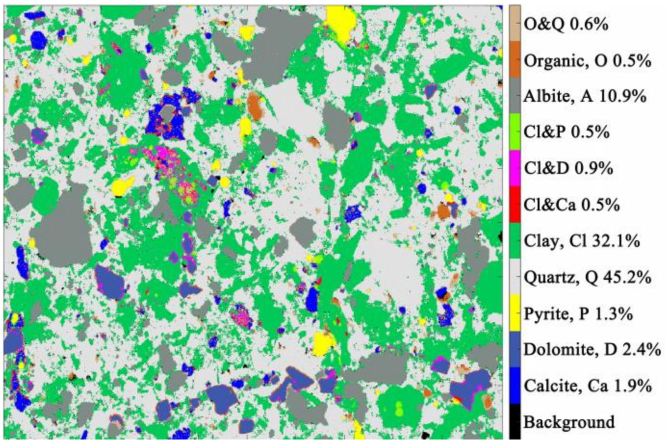

(c)

Fig. 5. Digital mineral maps of three Longmaxi shale samples across a 240 μm × 300 μm region: (a) Sample #1 (Carbonate-rich), (b) sample #2 (Clay-rich), and (c) sample #3 (quartz-rich).

2.4. Hydrothermal reaction system

In order to simulate the actual temperature and pressure conditions in the Longmaxi shale formation, an HT reaction system was set up to treat the samples (Fig. 6). The formation temperature and pressure gradually ramp up with increasing depth (He et al., 2019), with a ground temperature gradient and pressure coefficient of ~3 °C/100 m (Ren et al., 2007) and ~1 MPa/100 m (Huang et al., 2020), respectively. The depth of the Longmaxi shale formation ranges from less than 700 m to thousands of meters (Li et al., 2023a). It is noted that both the temperature and pressure are selected within the typical ranges for Longmaxi shale formation but may not correspond to the same depth. Therefore, based on the commonly used temperature and pressure values for Longmaxi shale formation in existing literature (Pan et al., 2016; Cheng et al., 2020), 80 °C and 8 MPa were adopted as the temperature and pressure conditions in the HT reaction system. In the treatment with water-based solutions, the fluid-to-rock mass ratio for all samples was ~10:1. The DI water and KCl solution were not deoxygenated, and contained a small volume of dissolved O_2 (~0.1 mL). All samples were treated with an exposure duration of 7 d. Alterations in the mechanical, morphological, and mineralogical properties for each treatment were evaluated by comparing the results of grid micro-indentation measurements and SEM/BSE-EDS scanning on the specimen before and after the treatment. In hydraulic fracturing, addition of 2% KCl is usually assumed for water-based fracturing fluids to enhance the gas recovery rate and maintain wellbore stability (Cheng, 2012). In this study, we measure and compare the effects of three different fluids (i.e. DI water, KCl brine, and $ScCO_2$) on mechanical degradation of carbonate-rich specimens of Longmaxi shale (CA1-CA5) at various pressures and temperatures (see Table 2). As limited specimens were obtained from clay-rich and quartz-rich Longmaxi shale samples, clay-rich and quartz-rich specimens (C1 and Q1) were only treated with DI water at elevated temperature and pressure (80 °C and 8 MPa) to enable direct comparison of the effects of shale mineralogy on mechanical degradation (CA3, vs. C1 and Q1; Table 2).

Fig. 6 shows the HT reaction system established in this study for treating the Longmaxi shale samples. First, an intact shale sample is placed in a ceramic cup and then immersed into the fluids (i.e. DI water or 2% KCl solution, Fig. 6a). Then, the ceramic is put into the air-tight reactor, which is carefully sealed (gasket and flange, Fig. 6b). Finally, a heating belt controlled by a thermal controller is assembled within the air-tight reactor to provide the target pressure and temperature (Fig. 6c). In the treatment with water-based solutions, a Nitrogen tank is connected to pressurize N_2 into the air-tight reactor to soak the shale specimens under the target pressure. In the treatment with $ScCO_2$, an amount of solid CO_2 (dry ice) was weighted based on the density of $ScCO_2$ at 80 °C and 8 MPa and the volume of the reactor (Lahann et al., 2013). Then, the dry ice and intact shale sample were placed into the reactor together, and the temperature inside the reactor was maintained at 80 °C by the thermal controller. The final pressure inside the reactor was measured at 8 MPa. According to the critical temperature and pressure of $ScCO_2$ (31 °C, 7.38 MPa), the CO_2 inside the reactor was in the supercritical state. In the treatment with both water-based solutions and $ScCO_2$, there was around 20 mL residual air in the sealed reactor, accounting for ~1% of the total mass of the $N_2/ScCO_2$ phase presented in the treatments. Before treating the shale samples, the HT reaction system was checked for pressure leaks. If the pressure measured by the pressure gauge showed a decrease within the accuracy range of the gauge over 24 h, it was determined that there were no leaks in the system.

Table 2

Summary of the test program.

Specimen ID	Fluid	Temperature (°C)	Pressure (MPa)	Duration (d)
CA1_int	-	20	0.1	7
CA1_de	DI water	20	0.1	7

CA2_int	-	20	0.1	7
CA2_de	2% KCl	20	0.1	7
CA3_int	-	20	0.1	7
CA3_de	DI water	80	8.0	7
CA4_int	-	20	0.1	7
CA4_de	2% KCl	80	8.0	7
CA5_int	-	20	0.1	7
CA5_de	ScCO$_2$	80	8.0	7
C1_int	-	20	0.1	7
C1_de	DI water	80	8.0	7
Q1_int	-	20	0.1	7
Q1_de	DI water	80	8.0	7

Note: CA, C, and Q denote the carbonate-rich, clay-rich, and quartz-rich samples, respectively. The intact carbonate-, clay-, quartz-rich shale samples are named as CA1_int, CA2_int, …; C1_int, …; and Q1_int, …, respectively. The treated carbonate-, clay-, and quartz-rich shale samples are named as CA1_de, CA2_de, …; C1_de, …; and Q1_de, …, respectively.

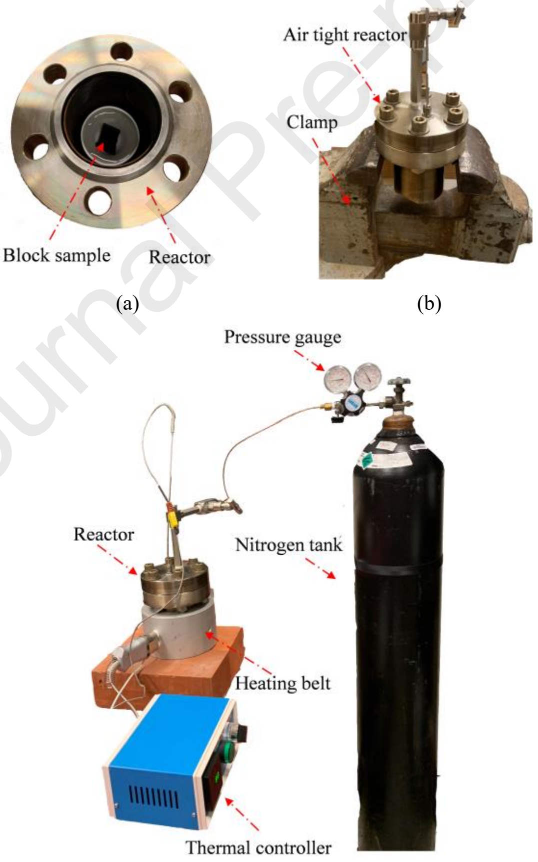

(a) (b)

(c)

Fig. 6. Hydrothermal reaction system: (a) immersing the intact shale sample into fluids, (b) sealing the air-tight reactor with the gasket and flange, and (c) assembling the reactor with the Nitrogen cylinder, heating belt, and temperature controller to provide the designated pressure and temperature.

2.5. Flowchart for the mesoscale analyses on the mechanical alterations induced by shale-fluid interactions

Fig. 7 shows the flowchart for the mesoscale analyses of mechanical alterations induced by shale-fluid interactions involving five steps:

(1) Step 1. The carbonate-, clay- and quartz-rich shale samples are carefully polished with mechanical polishing, and a series of grid micro-indentation tests are then performed at the length scale of the elementary building block of the bulk shale (8 -10 μm in this study) to assess the mechanical properties of the intact bulk shale.

(2) Step 2. SEM/BSE imaging and EDS scanning are conducted on the region of interest (ROI) (i.e. the grid micro-indentation region) for each intact shale sample to characterize the in situ mineralogy and surface morphology of the ROI.

(3) Step 3. The intact shale samples are treated with different fluids (i.e. DI water, 2% KCl solution, and $ScCO_2$) under different pressures and temperatures for 7 d.

(4) Step 4. After each treatment, SEM/BSE imaging and EDS scanning are performed over the same ROI located in the intact sample for a comparative analysis of the surface morphology and mineralogy before and after a specific treatment.

(5) Step 5. As the shale-fluid interactions increase the surface roughness, the treated samples are carefully re-polished to achieve a smooth surface before performing grid micro-indentation tests.

It is noted that based on the color change between the zone with water infiltration and the intact zone, SEM/BSE imaging has been conducted to confirm that the surface removed by re-polishing is shallow enough (hundreds of nanometers to a few micrometers) compared to the depth of the shale-fluid interaction zone (hundreds of micrometers). Finally, the mechanical alterations caused by the shale-fluid interactions are evaluated based on grid micro-indentation measurements before and after each treatment, and the corresponding mechanisms are then uncovered according to the microstructural and mineralogical changes observed from the in situ morphological and mineralogical identification technique.

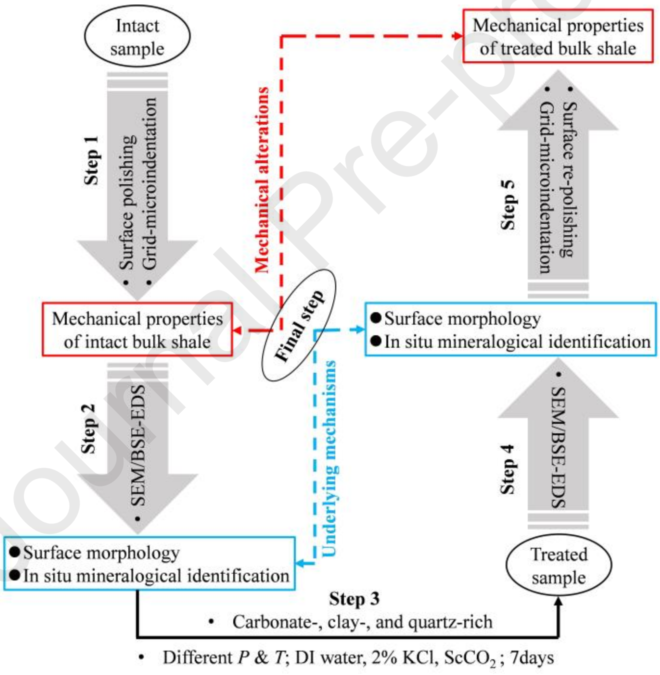

Fig. 7. Flowchart for mesoscale analyses of mechanical alterations induced by shale-fluid interactions.

3. Results

3.1. Mechanical alterations under different temperatures and pressures

Fig. 8 compares the statistical results of the grid micro-indentation measurements before and after treatment of DI water and 2% KCl brine under ambient room temperature (20 °C) and atmospheric pressure (0.1 MPa) and under the elevated temperature and pressure (i.e. 80 °C and 8 MPa). The data are presented in a raincloud format (Allen et al., 2019), combining conventional boxplots with interpretations based on the assumption of normal distribution function for each phase. The statistical mean, μ, and standard deviation, σ, of each distribution, are presented in the inset of each figure. The relative decrease in E and H is calculated by $(E_{int} - E_{de})/E_{int}$ and $(H_{int} - H_{de})/H_{int}$, respectively, where E_{int} and E_{de} and H_{int} and H_{de} are the Young's moduli and hardness of the intact and treated samples, respectively.

The results show that there are no apparent changes in the mechanical properties of the specimens treated with DI water and 2% KCl brine at room temperature and atmospheric pressure. In contrast, at elevated pressure and temperature, a 31.2% decrease in E and a 37.5% decrease in H were observed for the treatment of DI water, and a 6.5% decrease in E and a 16.4% decrease in H were observed for the treatment of 2% KCl brine. This indicates that increased pressure and temperature can accelerate mechanical alterations of shale formation. Evidently, in the deep underground with elevated temperature and pressure, the brittleness and fracability of shale formations will be significantly decreased (Rickman et al., 2008) after the water-based fracturing fluids are injected, which in turn impairs the performance of hydraulic fracturing.

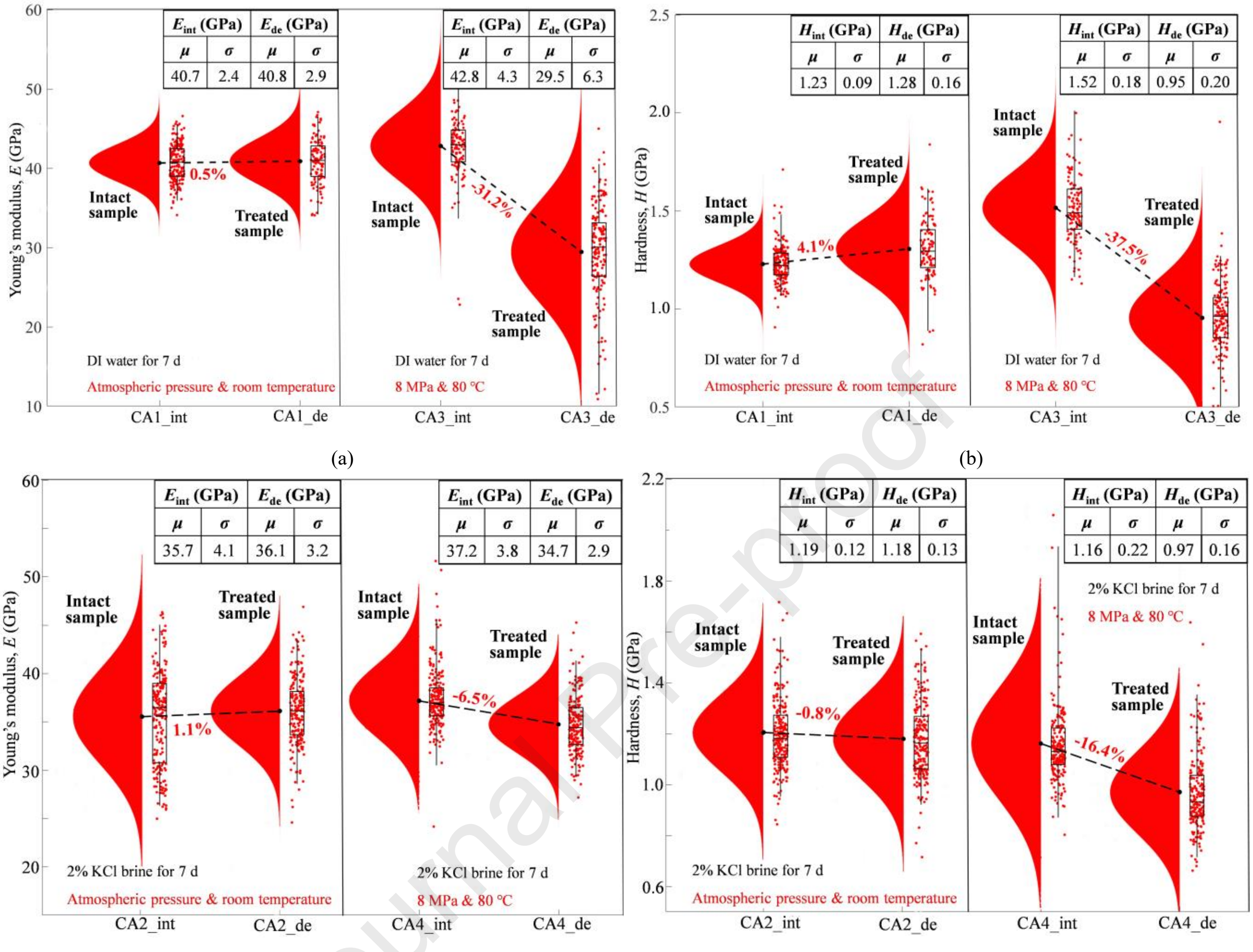

(a) (b)

(c) (d)

Fig. 8. Young's modulus and hardness alterations under room temperature and atmospheric pressure and under 80 °C and 8 MPa conditions: (a) and (b) treatment of DI water; and (c) and (d) treatment of 2% KCl brine. The locations of the statistical mean, μ, are indicated by black dots at the bottom of each distribution.

Surface morphology and mineralogy of the same ROI of a shale specimen are measured using the in situ morphological and mineralogical identification technique (see Section 2.3) before and after each treatment. Fig. 9 shows the mineralogical and morphological changes across the same ROI of the (carbonate-rich shale) specimen CA1 due to exposure to DI water for 7 d under different temperatures and pressures. The specimen surface is significantly eroded, especially after DI water treatment under high temperature and pressure. With elevating temperature and pressure, larger holes and voids are generated in the eroded surface, indicating that surface erosion can be significantly aggravated by the increased temperature and pressure. According to the spatial distribution of each mineral phase obtained from the digital mineral map (see Fig. 9), the representative particles of different mineral phases are circled out in the BSE images (using the corresponding color of each miner phase presented in the digital mineral map). It is found that the generated holes and voids in the eroded surface correspond to the locations of the carbonate minerals. In contrast, no apparent erosion is observed for the pyrite, quartz, and clay phases. Therefore, it is concluded that surface erosion or the generation of holes and voids is mainly caused by carbonate dissolution into the DI water.

To further reveal the effects of the elevated temperature and pressure on surface erosion, the surface morphology of carbonate-rich specimens CA1 and CA3 were compared. The two specimens were treated with DI water for 7 d at room temperature, atmospheric pressure, and at 80 °C and 8 MPa, respectively. Fig. 10 shows the surface morphology of the intact and degraded specimens measured by the BSE imaging and the microscale void ratios analyzed with the image processing technique, which has been extensively used in investigation of the porosity of composite materials (e.g. rocks and concrete) (Kaestner et al., 2008; Elia et al., 2016; Liu et al., 2022; Tang and Gratchev, 2023). The voids in the regions of interest are extracted by conducting a threshold algorithm of grayscale with Matlab coding (highlighted with red color in Fig. 10). After exposure to DI water for 7 d, specimen CA3 (see Fig. 10d) exhibits a more severe surface erosion compared with that of the specimen CA1 (Fig. 10b). The measured void ratios (i.e. area fraction of the red color in each figure) of CA1 and CA3 were increased from 2.6% to 5.8% and from 1.8% to 9.7%, respectively. These results show that elevated temperature and pressure exacerbate the carbonate dissolution into the water-based solutions, and thus lead to significant alterations in rock structure and mechanical properties. The carbonate minerals can dissolve into the neutral and alkaline aqueous solutions, driven by the following reaction (Chou et al., 1989):

$$MCO_3+H_2O \longrightarrow M^{2+}+HCO_3^-+OH^- \quad (5)$$

where M represents the metal ion (e.g. Ca^{2+}, Mg^{2+}). For a two-component carbonate mineral, e.g. dolomite ($CaMg(CO_3)_2$), Busenberg and Plummer (1982) interpreted the driven mechanism of the dissolution by a two-step reaction. The $CaCO_3$ component dissolves faster, and the surface composition becomes enriched with the $MgCO_3$ component. The first step is relatively rapid, and the dissolution rate of the two-component carbonate mineral is thus controlled by the rate of the second step. This may account for the observation of the more severe erosion of calcite mineral compared with the dolomite mineral (see Fig. 9).

The effects of temperature on the dissolution kinetics of carbonates have been studied as a function of pH and temperature (Plummer et al., 1978; Carroll and Knauss, 2005). In neutral and alkaline environments, carbonate dissolution occurs in an H^+-independent regime characterized by mixed kinetics, i.e. product diffusion through the diffusive boundary layer (DBL) and a first-order surface chemical reaction. The former process is facilitated by increasing the temperature. Gutjahr et al. (1996) found that the rate constant of calcite dissolution ranged from 1×10^{-10} mol cm^{-2} s^{-1} to 2×10^{-10} mol cm^{-2} s^{-1} at temperature of 20-70 °C. Kirstein et al. (2016) observed that the dissolution rate of limestone, a sedimentary rock mainly composed of calcite and dolomite, can be increased by up to 5 times when the temperature increases from 5 °C to 26 °C. Gong et al. (2008) measured the dissolution rate of calcite exposed to deionized water at varying temperatures of 50 °C to 250 °C and a pressure of 10 MPa. The measured dissolution rate was described using an exponential function with a temperature-dependent order.

Carbonate dissolution is also influenced by hydrodynamic factors, such as hydrodynamic pressure. The effects of hydrodynamic pressure in the rock reservoir on the dissolution rate of carbonate minerals have been studied recently. Meng et al. (2022) conducted a series of carbonate rock dissolution tests under varying hydrodynamic pressures (2 MPa to 6MPa). The dissolution rate was found to be proportional to the applied hydrodynamic pressure. Liu et al. (2013) studied the dissolution mechanisms of limestone driven by hydrodynamic reservoir pressure. The measured dissolution rate increased with elevated hydrodynamic pressure and temperature. The mechanical damage, such as the generation of cracks and voids, was raised to be responsible for the increase in dissolution rate. Moreover, the fluid infiltration is enhanced by the increased hydrodynamic pressure, which results in a larger contact between carbonate minerals and fluids and thus augments the carbonated dissolution rate. As the temperature and pressure conditions vary significantly with depth in the shale formation, further studies are needed to characterize the relationship between mechanical/mineralogical alterations over various temperatures and pressures.

Deposition and sedimentation of the Longmaxi shale occurs in a marine environment, enabling cementation and carbonate diagenesis (Feng et al., 2023). Carbonate minerals, i.e. the combination of calcite and dolomite, may serve as the inter-grain cementing agents of the studied Longmaxi shale samples (see Figs. 2 and 9). Therefore, carbonate dissolution upon injection of the water-based fluids acts both to increase the porosity of the shale and to weaken the cementing bonds between grains of the rock. Both of these processes are expected to cause significant degradation in the mechanical properties of shale. Chen et al. (2023) conducted a numerical study on the effects of porosity and inter-grain cementation on the elastic properties of sandstone. A three-dimensional (3D) finite element model with inter-grain boundaries modelled by cohesive elements was used. The increase of porosity and weakening of the inter-grain cementation accounted for 33.3% and 49.7%of the reduction in Young's modulus, respectively.

Most current studies have emphasized the mechanical degradation induced by the carbonate dissolution in the acid solutions environment. For instance, Pimienta et al. (2017) investigated the carbonate dissolution induced by CO_2-brine-rock interactions and the effects on the rock's mechanical properties. Significant porosity increase and mechanical weakening were observed after only 2 h of exposure. However, limited attention has been drawn to the mechanical degradation by water-based solutions only, especially under the subsurface conditions of high temperature and pressure.

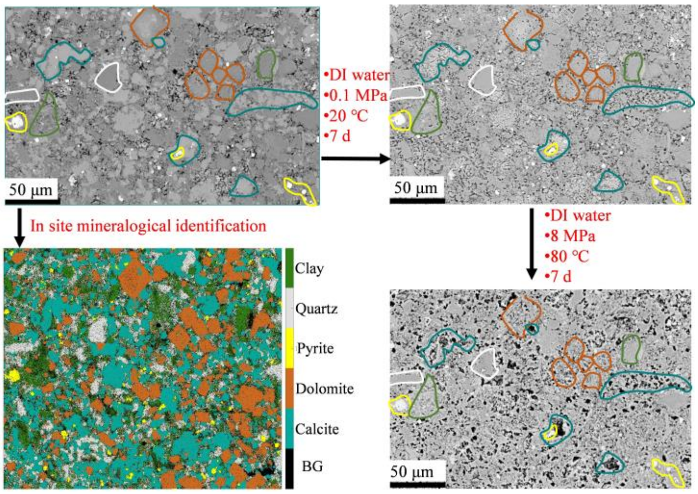

Fig. 9. Mineralogical and morphological changes across the same ROI of the carbonate-rich shale specimen CA1 due to the exposure to DI water for 7 d under different temperatures and pressures. Representative particles of different mineral phases are circled out in the BSE images using the corresponding color of each miner phase presented in the digital mineral map. The label 'BG' in the digital mineral map denotes the background of the map, i.e. blank pixels with no mineral phases identified.

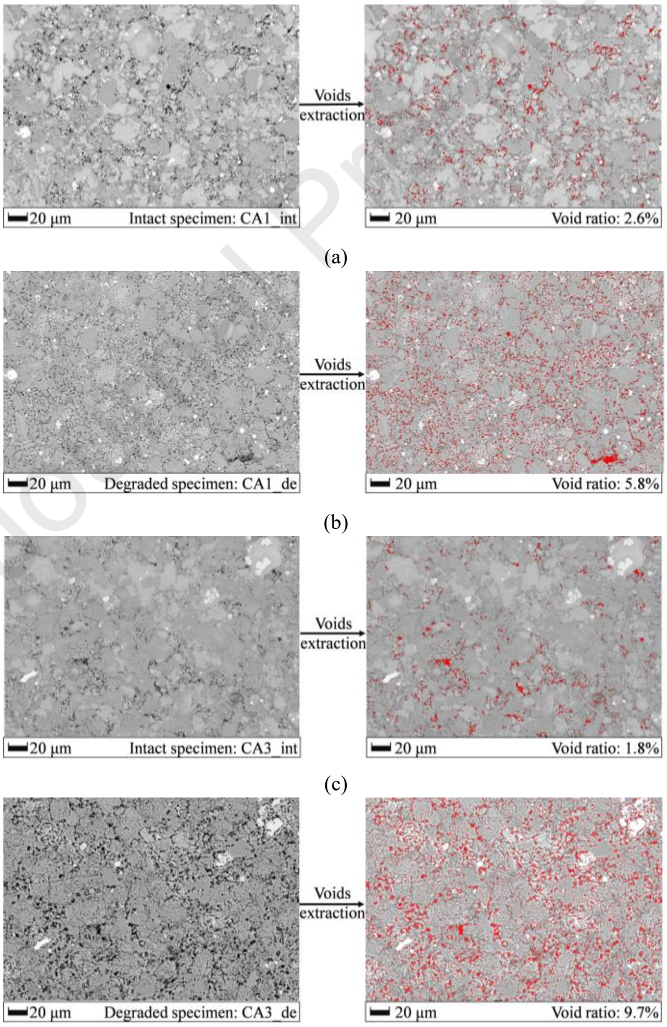

(a)

(b)

(c)

(d)

Fig. 10. Alterations of surface morphology and microscale void ratios of specimens CA1 and CA3, which were treated with DI water for 7 d at room temperature and atmospheric pressure and at 80 °C and 8 MPa, respectively. (a) and (c) show the surface morphology and microscale void ratio of intact specimens CA1 and CA3, respectively; (b) and (d) show the surface morphology and microscale void ratio of degraded specimens CA1 and CA3, respectively.

3.2. Mechanical alterations induced by the treatment of different water-based solutions

To evaluate the effect of the addition of KCl on the mechanical degradation of Longmaxi shale samples, mechanical alterations caused by the treatment with DI water and 2% KCl brine (specimens CA3 and CA4, respectively) at elevated temperature and pressure conditions are compared in Fig. 11. With addition of 2% KCl into DI water, the degradation of *E* and *H* was ameliorated by about 80% and 60%, respectively. The results show that KCl effectively mitigates mechanical degradation caused by the injection of water-based fracturing fluids into the carbonate-rich Longmaxi shale formation.

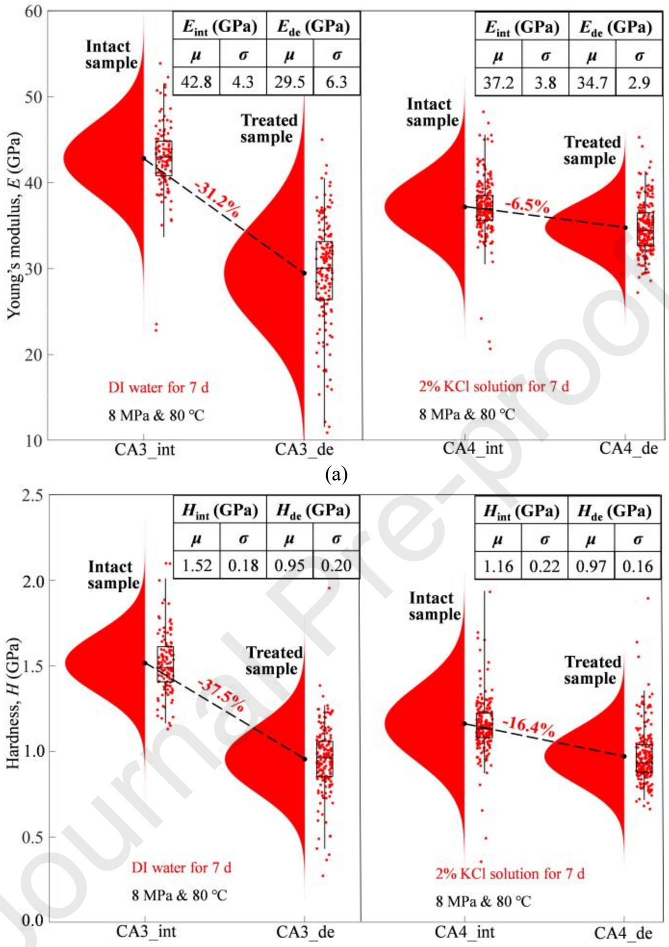

(a)

(b)

Fig. 11. Mechanical property alterations induced by the treatment with DI water and 2% KCl brine: (a) *E*, and (b) *H*.

When in contact with aqueous liquids, some clay minerals undergo crystalline swelling due to the intercalation of water between primary clay particles (Foster et al., 1955; Zhang and Low, 1989); while others, such as illite (the primary clay mineral found in the studied Longmaxi shale samples), exhibit osmotic swelling when the aqueous fluid has a lower cation concentration, due to the repulsion between electrical double layers. (Du et al., 2018). The clay-fluid interactions have been recognized to be the primary cause of shale instability (Mody and Hale, 1993; Al-Awad and Smart, 1996; Lal, 1999). O'Brien and Chenevert (1973) classified the instability of shales into five main categories based on their clay mineral composition. Wong (1998) studied the swelling and softening behavior of La Biche shale after soaking it in water and NaCl solutions for up to 140 d. The shale swelling was found to decrease with increasing solution salinity, while the Young's modulus decreased with increasing swelling, following a descending power law

$$E_{\mathrm{d}} = E_{\mathrm{i}}[1-(\varepsilon_{\mathrm{v}} / \varepsilon_0)^k] \qquad (6)$$

where E_d and E_i denote Young's modulus of degraded and intact samples, respectively; ε_v is the volumetric strain; ε_0 is the normalized volumetric strain constant (ε_0 = 25%); and k is a constant, and $k = 0.3$.

By conducting the Brinell hardness tests, Lafollette and Carman (2013) found a decrease of up to 87% in the Brinell hardness of shale containing 56% illite after exposure to acetic acid or a KOH/K_2CO_3 solutions for 120 d. Liu et al. (2021) exposed a mudstone consisting of quartz (20.09%), illite (30.51%), kaolinite (36.93%), and chlorite (12.48%) to water for 15 d. Consequently, a swelling strain of ~6% was observed, and the uniaxial compressive strength and elastic modulus of the treated samples were found to be reduced by a maximum of 81.74% and 80.37%, respectively. It has been proven that clay swelling accounted for the mechanical degradation of clay-rich shales after exposure to aqueous fluids.

Besides the concentration of cations in the injected aqueous fluids (Wang and Rahman, 2015), the cation hydration complex, which can be classified as either inner-sphere or outer-sphere (Sposito, 1989), also exhibited significant influence in the osmotic swelling. An inner-sphere hydration complex is formed when no water molecules exist between the surface functional groups and small cations or molecules. In contrast, an outer-sphere hydration complex is formed if at least one interposed water molecule is present between the surface functional group and small cation. Boek et al. (1995) and Anderson et al. (2010) found that Li^+ and Na^+ cations can form outer-sphere complexes upon the addition of water and thus showed a tendency to migrate away from the sheet surface and fully hydrate, while K^+ cation only formed inner-sphere complexes that constrained its migration to the clay sheet surface and further hydration. As such, with the addition of Li^+ and Na^+ cations, osmosis takes place between the layers as well as between the particles, in contrast to K^+ cation, osmosis occurs only between the particles.

Grid micro-indentation measurements in this study showed that the mechanical degradation is significantly mitigated by 2% KCl additive (see Fig. 11). This can be attributed to the reduction in osmotic repulsion of 2% KCl vs. DI water and the action of K^+ cations in the formation of inner-sphere complexes which inhibit the intake of water between clay platelets (Du et al., 2018).

3.3. Mechanical degradation of shales with different mineralogy

The mineralogy of a shale formation affects its mechanical properties (E, H) and its response to fluid treatments. Fig. 12 compares the mechanical degradation in the three Longmaxi shale samples with three distinct mineralogies (i.e. carbonate-, clay-, and quartz-rich; CA3, C1, and Q1) due to treatment with DI water at 80 °C and 8 MPa, the Young's modulus was decreased by 31.2%, 23.9%, and 11.4%, and hardness was decreased by 37.5%, 16.0%, and 5.9% for the carbonate-, clay-, and quartz-rich shale samples, respectively. The results indicate that carbonate-rich shale formations are the most sensitive to the water-based fracturing fluids, followed by the clay-rich and quartz-rich shale formations.

As mentioned above, clay has been generally recognized as a causative mineral attributed to the swelling and mechanical weakening of shale after exposure to aqueous fluids. Observations in the present study indicate that caution is required when using water-based fluids to fracture a formation rich in carbonate minerals. This is because the carbonate dissolution will be exacerbated under the subsurface conditions of high temperature and pressure, thus increasing the porosity and weakening the inter-grain cementation of shale. Fig. 13 shows the relationship between the decrease in the Young's modulus, hardness and the total clay and carbonate minerals content of the three shale samples. For specimens C1 and Q1, both of which are carbonate-depleted (i.e. samples #2, and #3 in Table 1, both with carbonate content ~3%), the aggravated mechanical degradation of C1 compared to Q1 is mainly attributed to the higher clay content. Therefore, the data provide a means to evaluate the roles of clay content in mechanical degradation. With the clay content increased from 29.2% to 44.8%, the decrease of the Young's modulus and hardness was changed from -11.4% to -20.2% and from -5.9% to -16%, respectively. Whereas, for specimens CA3 and Q1, which have similar clay content (samples #1, and #3 in Table 1, 26.8% and 29.2%, respectively), the aggravation of mechanical degradation was dominated by increase of the carbonate content. With the carbonate content increased from 3.4% to 40.7%, decrease of the Young's modulus and hardness was changed from -11.4% to -31.4% and from -5.9% to -37.5%, respectively. Fig. 13 summarizes the mechanical degradation, ΔE and ΔH, as a function of the combined clay and carbonate content. The gradients of the red and blue lines represent the mechanical degradation induced per unit change in clay and carbonate content, respectively. With the same amount of clay and carbonate minerals, the Young's modulus exhibited an equivalent degradation, whereas hardness appeared to be more sensitive to carbonate dissolution. In consideration of clay and carbonates as the equivalent causative minerals for mechanical degradation induced by exposure to water-based solutions at elevated temperature and pressure, the decrease of both Young's modulus and hardness were correlated with the total content of clay and carbonate minerals, and a linear relationship can be obtained (see black dotted lines in Fig. 13, with $R^2 = 0.999$ and 0.974, respectively).

The intercepts on the x-axis may reflect a lower limit on the clay and/or carbonate content to trigger measurable mechanical degradation. If this is the case, the mechanical properties of the bulk shale are only affected when the fraction of the degrading constituent phase exceeds ~5 wt.% (Sreekanth et al., 2009). On the other hand, the current tests measure degradation for a fixed treatment duration (7 d). It is also possible that prolonged exposure will increase the measurable degradation. Overall, it can be concluded that when exposed to water-based solutions under subsurface conditions of elevated temperature and pressure, clay and carbonate minerals can cause comparable mechanical degradations. In that framework, the total content of clay and carbonate minerals can be a useful index of the potential degradation of a shale formation by water-based fracturing fluids.

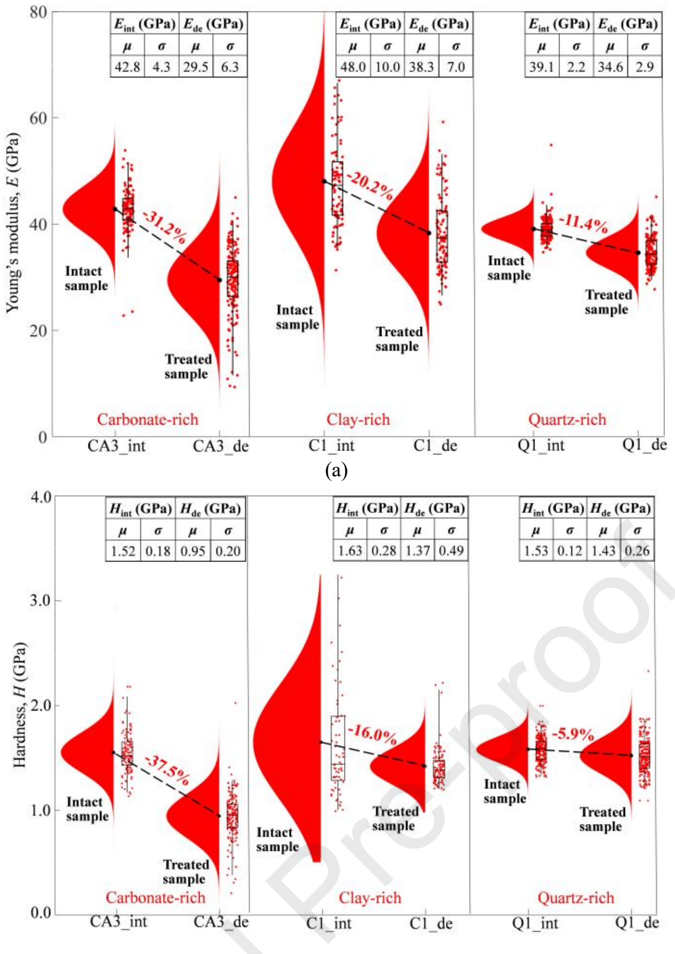

(a)

(b)

Fig. 12. Comparison of the mechanical degradation among the carbonate-, clay-, and quartz-rich shale samples after the treatment with DI water under 80 °C and 8 MPa: (a) *E*, and (b) *H*.

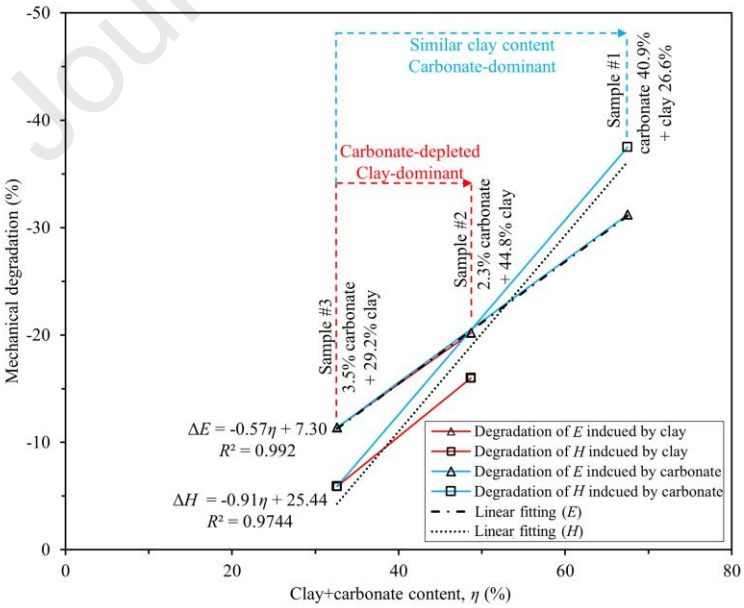

Fig. 13. The relationship between the decrease in the Young's modulus and hardness and the content of clay and carbonate minerals for 7-d exposure treatment.

3.4. Mechanical alterations induced by the exposure to $scCO_2$

The effects of exposure to $ScCO_2$ have been reported to induce complex physical and mineralogical changes in shale, including adsorption-induced swelling (Lu et al., 2016; Liu and Liu, 2022) and pressure-induced matrix compression (Pan and Connell, 2007; Vandamme et al., 2010). Both Pan and Connell (2007) and Vandamme et al. (2010) revealed that after injection of $ScCO_2$, swelling behavior initially follows the adsorption isotherm. However, at higher pressures, the dominant effect gradually shifts to matrix compression, which results in a reduction in volumetric strain. Furthermore, Espinoza and Santamarina (2012) found that the van der Waals attraction between clay minerals is increased in the $ScCO_2$ fluid due to the dielectric properties of CO_2, which in turn may give rise to a more compact clay matrix with a smaller porosity. The competition between these processes makes predicting the net mechanical degradation challenging.

In this study, the carbonate-rich shale specimen CA5 was immersed in pure $ScCO_2$ for 7 d. Fig. 14 shows the statistical results of the alterations in E and H induced by the exposure to $scCO_2$. The results show small increases in both E and H (i.e. 3.1%, 3.3%, respectively) due to $ScCO_2$ treatment at elevated pressure and temperature. Similar observations were reported in previous studies. Indeed, Yin et al. (2017) reported a slight increase in the uniaxial compressive strength of shale after soaking in the $ScCO_2$ for 10 d. They attributed this phenomenon to the shale matrix compression under high-pressure conditions. Moreover, Guo et al. (2018) studied the effect of $ScCO_2$ soaking pressure on the mechanical properties of shale and reported an increase in the Young's modulus and Poisson's ratio caused by the shrinkage of the clay component. However, using a nano-indentation technique, Liu et al. (2023) concluded a non-monotonic change in the mechanical properties of shale after exposure to $ScCO_2$ for 60 d. The measured fracture toughness and contact creep modulus initially increased during 0-8 d, then decreased during 8-16 d, and finally increased again during 16-60 d. This indicated that the exposure time may play a significant role in the effect of the competition between the swelling caused by adsorption and the pressure-induced matrix compression on the mechanical behavior of shale.

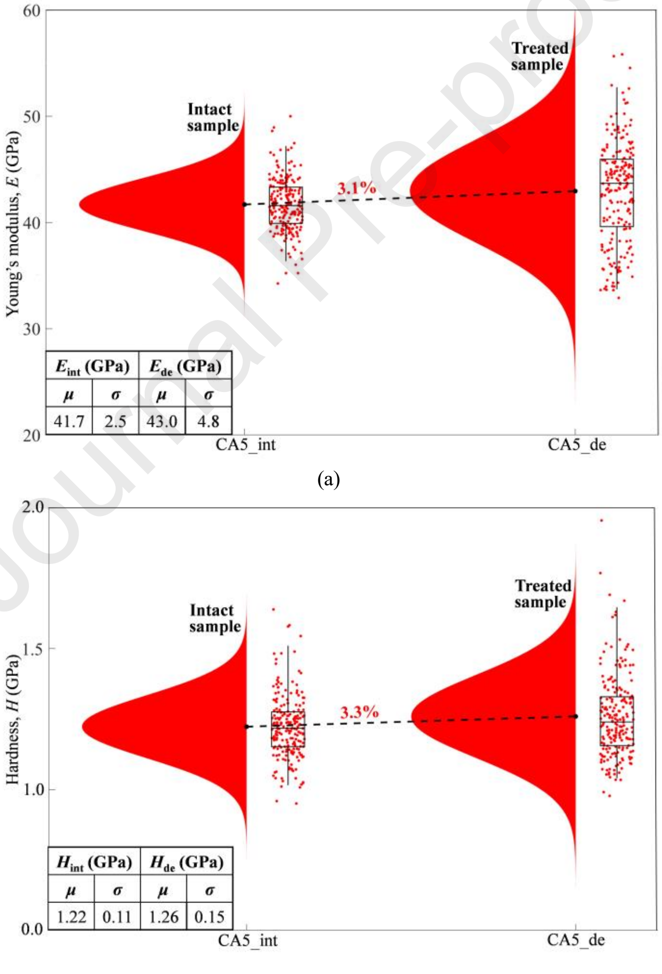

(a)

(b)

Fig. 14. Mechanical alterations induced by the exposure to $ScCO_2$ for 7 d: (a) E, and (b) H.

Fig. 15 shows the measured microstructure and mineralogy in the same ROI before and after the shale specimen CA5 is treated with $ScCO_2$ for 7 d. It shows that the porous clay matrix (circled by a white dashed line) became more compact after the 7-d exposure treatment. The area of interparticle voids (encompassed by red lines) was clearly decreased after the exposure to $ScCO_2$ for 7 d. The microscale porosity of the red circled regions is further analyzed with an image processing technique, which has been extensively used in investigation of the porosity of composite materials (e.g. rocks and concrete) (Kaestner et al., 2008; Elia et al., 2016; Liu et al., 2022; Tang and Gratchev, 2023). The voids in the regions of interest are extracted by conducting a threshold algorithm of grayscale with a Matlab code (highlighted in red in Fig. 15c and d). After exposure to

$ScCO_2$ for 7 d, the measured void ratio (i.e. the area fraction of the red color in Fig. 15c and d) decreases from 32.2% to 24.8%, indicating a more compact clay matrix of the treatment sample compared to the intact sample. This microstructural observation may account for the slight increase in *E* and *H* measured in this study. The yellow circles in Fig. 15a and b highlight the local surface subsidence formed by the residual footprint of the indentation, which is located in the porous matrix. With compressed matrix, the inner pores of the matrix were squeezed, and the particles coalesced, which may make this local surface subsidence more visible.

Future research efforts are needed to investigate the impact of the competition between the adsorption-induced swelling and the shale matrix compression on the long-term mechanical behavior during the interaction between shale and $ScCO_2$. Further studies are also needed on the shrinkage of meso/micro-scale pores within the clay matrix (Desbois et al., 2009; Clarkson et al., 2013; Mathia et al., 2019). Comparison of the pore size structure before and after treatment can be achieved using gas physisorption analyses (e.g. nitrogen or carbon dioxide adsorption) (Han et al., 2017; Yang and Liu, 2020), which can provide more evidence on the underlying mechanisms controlling the mechanical alteration induced by $ScCO_2$ exposure.

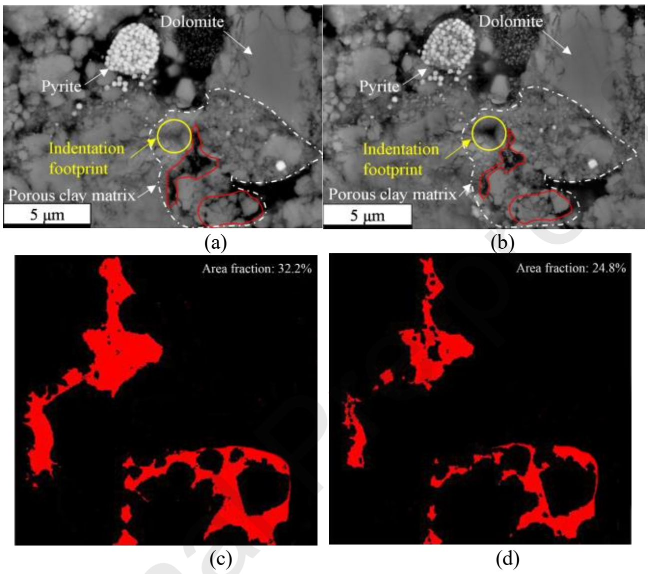

Fig. 15. Measured microstructure and mineralogy in the same ROI of shale specimen CA5: Mineralogy (a) before and (b) after the treatment with $ScCO_2$ for 7 d, and microscale porosity of the interested regions (red circled in (a) and (b)) (c) before and (d) after the treatment with $ScCO_2$ for 7 d.

4. Discussion

4.1. Pyrite oxidation

Another mineral-fluid reaction that may contribute to the alterations of shale mechanical properties is the oxidation of pyrite (FeS_2). The dissolved O_2 in the solutions can be the oxidant for the aqueous oxidation of pyrite (Holmes and Crundwell, 2000; Dos Santos et al., 2016; Feng et al., 2019). Chemical reactions of the aqueous oxidation of pyrite can be described as follows (Chandra and Gerson, 2010):

$$FeS_2 + 3.5O_2 + H_2O = Fe^{2+} + 2SO_4^{2-} + 2H^+ \quad (7)$$

$$FeS_2 + 14Fe^{3+} + 8H_2O = 15Fe^{2+} + 2SO_4^{2-} + 16H^+ \quad (8)$$

Sulfuric acid, a product of pyrite oxidation, can react with carbonate minerals and consequently enhance their dissolution into aqueous solutions. Pyrite and carbonate minerals are the most common constituent phases of shale. Thus, as pyrite and carbonate minerals coexist, the aqueous oxidation of pyrite will deteriorate the mechanical degradation of shale. As shown in Fig. 16, the calcium sulfate crystals ($CaSO_4$) were observed on the surface of the carbonate-rich Longmaxi shale sample after treatment with DI water for 7 d. The calcite particles were also observed to be significantly broken down due to increased acidity. This observation implies the reaction of the calcite mineral with the sulfuric acid produced by pyrite oxidation. Besides the dissolved O_2, Fe^{3+} has also been recognized as an important oxidant for aqueous oxidation of pyrite (Li et al., 2023b). Therefore, considering the oxidants carried by the fracturing fluids adding into the oxygen-free subsurface environment, a deoxygenation treatment for fracturing fluids may need to be conducted, especially for locations abundant with pyrite minerals.

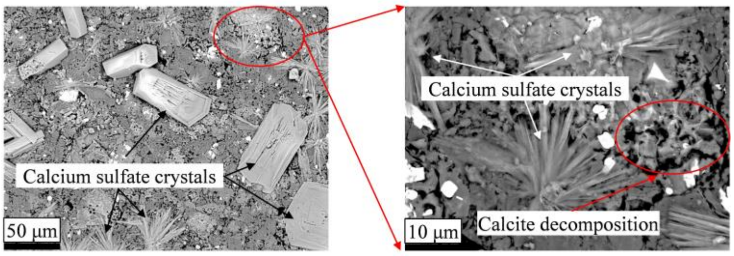

Fig. 16. BSE micrographs of the surface erosion caused by pyrite oxidation. Massive calcium sulfate crystals ($CaSO_4$) are generated on the surface after treatment with DI water for 7 d. Significant breaking down is also observed for the calcite particles (red circled).

4.2. Compositional analysis of fluids post-reaction

The extent of the chemical reaction between minerals and injected fluids governs the induced alterations in mechanical and mineralogical properties. In principle, fracture fluid recipes should be tailored specifically to the mineral composition of each targeted shale reservoir to enhance formation stimulation and gas recovery. As observed in this study, at temperature and pressure conditions expected in the formation, short-term duration (7 d), can cause substantial dissolution of carbonate minerals into the injected water-based fluids. This process is potentially exacerbated by pyrite oxidation (Eqs. (5), (7), and (8)). In future work, a compositional analysis of the fluid post-reaction, such as Inductively Coupled Plasma-Optical Emission Spectrometry (ICP-OES) (Gundogar et al., 2022; Medina-Rodriguez et al., 2023), could provide an insightful assessment of the extent of the chemical reaction between minerals and injected fluids, and thus reveal the governing mechanisms for the observed mechanical degradation.

Moreover, for a carbonate-rich shale formation, inhibitors such as heavy-metal ions (scandium and copper) (Sjoberg, 1978; Sjöberg and Rickard, 1984; Zeppenfeld, 2010) can be considered as additives in the fracturing fluids to suppress the carbonate dissolution. The promotion of common-ion effect, which refers to the decrease in solubility of precipitate by addition of ions in common with the precipitate (Ayogu et al., 2020), should also be an effective measure to inhibit carbonate dissolution (Ding et al., 2021).

Here, it shows that the coupling analysis of grid micro-indentation and compositional identification of fluids post-reaction is a promising route to the governing mechanisms of observed mechanical degradation and, in turn, facilitates the screening of additives in the injected fluids to prevent the potential formation degradation.

4.3. Impacts of the observed mechanical and mineralogical alterations on engineering applications

The mechanical and mineralogical alterations induced by the shale-fluids interactions can significantly influence proppant embedment, matrix permeability, fracture conductivity, and fracability. Consequently, they can substantially impact shale gas exploration and long-term production. Given the very low permeability of many shale formations, the capability of being fractured, also termed 'fracability', is critical for gas production (Jarvie et al., 2007). Current exploration practices use the brittleness index proposed by Rickman et al. (2008) (a function of Young's modulus and Poisson's ratio) to evaluate the fracability of shale formations (Kang et al., 2020). The Young's modulus and Poisson's ratio reflect a rock's ability to maintain a fracture and fail under stress, respectively, and thus, shales with a high Young's modulus and a low Poisson's ratio are considered more brittle and, hence, more easily fractured (Zhang et al., 2016).

Re-fracturing the shale formation that has been hydraulically fractured before has been among the most used restimulation techniques (Shah et al., 2017). Reduction in gas production over time usually did not appear to be totally related to production depletion, and the older under-performing wells can be restored by re-fracturing to near original or even higher production rates with much less expenses than the construction of new wells (Dozier et al., 2003). However, as observed in this study, significant degradation in the Young's modulus (up to 31% reduction) was observed after treatment with DI water for only 7 d. Modifications in the brittleness of shale formations that water-based fluids have fractured need to be assessed in initial evaluation of re-fracturing fracability.

The effects of the induced mechanical and mineralogical alterations on the permeability can be twofold. On one hand, the dissolution of carbonate minerals increases the porosity, and thus leads to increase of the permeability. Alalli et al. (2018) conducted laboratory permeability measurements on shale samples from Eagle Ford and Marcellus reservoirs. The permeability of the two samples after being treated with an acidic fracturing fluid (at 80 °C and 7.7 MPa) for 6 d exhibited opposite trends. Many secondary pores were created in the Eagle Ford sample, resulting in an order-of-magnitude increase in permeability. In contrast, the accumulation of barite precipitation inside the limited microcracks of the Marcellus sample led to the occlusion of the main transport flow paths and reduced permeability. On the other hand, the carbonate precipitation (Khather et al., 2020) and the fines migration (Ellis et al., 2013) can cause clogging and occlusion of flow paths. Moreover, the additional proppant embedment caused by the mechanical degradation will reduce the fracture aperture and impair the permeability of fracture pathways (Katende, 2022; Katende et al., 2022). Therefore, the permeability evolution of hydraulically fractured shale formations may depend on the extent of mechanical and chemical alterations, including carbonate dissolution and precipitation, fines migration, and proppant embedment. A comprehensive experimental work on the permeability evolution during shale gas exploration will help predict the performance of the gas recovery.

5. Conclusions

This study presents a mesoscale analysis based on the statistical micro-indentation measurement and in situ morphological and mineralogical identification to assess the mechanical and mineralogical alteration of Longmaxi shales exposed to water-based fluids and $ScCO_2$. The findings quantify the mechanical and mineralogical degradation of shale in the subsurface environment and can facilitate the engineering design and operation of shale gas exploration and CO_2 geological sequestration. Key conclusions are drawn as follows:

(1) Significant mechanical degradation (a reduction of 31.2% and 37.5% in E and H, respectively) is observed after exposing the carbonate-rich shale sample to DI water under 80 °C and 8 MPa for 7 d, while no apparent degradation was shown for similar treatment at ambient conditions. The addition of 2% KCl into DI water effectively mitigates degradation to both E and H.

(2) Quartz-rich Longmaxi shale is the least sensitive to degradation in DI water, followed by the clay-rich and carbonate-rich Longmaxi shale. The total content of clay and carbonate minerals can be a useful index of the potential degradation of a shale formation by water-based fracturing fluids.

(3) Mechanisms for the mechanical degradation induced by water-based fluids mainly include carbonate dissolution and clay swelling. The carbonate dissolution can be exacerbated by elevated temperature and pressure, as well as pyrite oxidation.

(4) A small increase in the Young's modulus and hardness is observed after the treatment with ScCO2 for 7 d. The pressure-induced compression of porous clay aggregates may account for this observation.

In future works, a coupling analysis of grid micro-indentation and compositional identification of fluids post-reaction is promising to provide a better understanding of the governing mechanisms for the observed mechanical degradation and, in turn, facilitate the screening of additives in the injected fluids for prevention of the potential formation degradation. Moreover, though the short-term softening behavior of shale after exposure to water-based fluids and supercritical CO_2 is investigated in this study, it is recommended that this research can be expanded, and the mechanical degradation of shale over different time intervals can be examined.

Declaration of competing interest

The authors declare that they have no known competing financial interests or personal relationships that could have appeared to influence the work reported in this paper.

Acknowledgements

This research was funded by the Open Research Fund Program of State Key Laboratory of Hydroscience and Engineering (Project Number: sklhse-2023-D-04) and the National Natural Science Foundation of China (Grant Nos. 51979144, 51661165015, and 51323014). The research was conducted while Jianting Du was a visiting PhD student at MIT.

References

Abedi, S., Slim, M., Hofmann, R., Bryndzia, T., Ulm, F., 2016. Nanochemo-mechanical signature of organic-rich shales: A coupled indentation–EDX analysis. Acta Geotech. 11 (3), 559-572.

Akono, A.-T., Kabir, P., 2016. Microscopic fracture characterization of gas shale via scratch testing. Mech. Res. Commun. 78, 86-92.

Akono, A.-T., Randall, N.X., Ulm, F.-J., 2012. Experimental determination of the fracture toughness via microscratch tests: Application to polymers, ceramics, and metals. J. Mater. Res. 27 (2), 485-493.

Akono, A.T., Druhan, J.L., Dávila, G., Tsotsis, T., Jessen, K., Fuchs, S., Crandall, D., Shi, Z., Dalton, L., Tkach, M.K., 2019. A review of geochemical–mechanical impacts in geological carbon storage reservoirs. Greenhouse Gases Sci. Technol. 9 (3), 474-504.

Al-Awad, M.N., Smart, B., 1996. Characterization of shale-drilling fluid interaction mechanisms related to wellbore instability. J. King Saud Univ-Eng. Sci. 8 (2), 187-214.

Alalli, A., Li, Q., Jew, A., Kohli, A., Bargar, J., Zoback, M., Kovscek, A. 2018. Effects of hydraulic fracturing fluid chemistry on shale matrix permeability. In: SPE/AAPG/SEG Unconventional Resources Technology Conference. URTEC, D013S015R009.

Allen, M., Poggiali, D., Whitaker, K., Marshall, T.R., van Langen, J., Kievit, R.A., 2019. Raincloud plots: A multi-platform tool for robust data visualization. Wellcome Open Res. 4. https://doi.org/10.12688/wellcomeopenres.15191.1.

Anderson, R., Ratcliffe, I., Greenwell, H., Williams, P., Cliffe, S., Coveney, P., 2010. Clay swelling—A challenge in the oilfield. Earth Sci. Rev. 98 (3), 201-216.

Asahina, D., Pan, P., Tsusaka, K., Takeda, M., Bolander, J.E., 2018. Simulating hydraulic fracturing processes in laboratory-scale geological media using three-dimensional TOUGH-

RBSN. J. Rock Mech. Geotech. Eng. 10 (6), 1102-1111.

Ayogu, P., Ezugwu, M., Eze, F., 2020. Principle of Common-ion Effect and its Application in Chemistry: A review. J. Chem. Lett. 1 (2), 77-83.

Benge, M., Katende, A., Rutqvist, J., Radonjic, M., Bunger, A., 2023. Creep properties of shale and predicted impact on proppant embedment for the Caney shale, Oklahoma. Rock Mech. Rock Eng. 56 (8), 5903-5921.

Bobko, C.P., Gathier, B., Ortega, J.A., Ulm, F., Borges, L., Abousleiman, Y.N., 2011. The nanogranular origin of friction and cohesion in shale—A strength homogenization approach to interpretation of nanoindentation results. Int. J. Numer. Anal. Methods Geomech. 35 (17), 1854-1876.

Bobko, C.P., Ulm, F., 2008. The nano-mechanical morphology of shale. Mech. Mater. 40 (4), 318-337.

Boek, E., Coveney, P., Skipper, N., 1995. Monte Carlo molecular modeling studies of hydrated Li-, Na-, and K-smectites: Understanding the role of potassium as a clay swelling inhibitor. J. Am. Chem. Soc. 117 (50), 12608-12617.

Busenberg, E., Plummer, L.N., 1982. The kinetics of dissolution of dolomite in CO_2-H_2O systems at 1.5 to 65 degrees C and O to 1 atm P_{CO2}. Am. J. Sci. 282 (1), 45-78.

Carroll, S.A., Knauss, K.G., 2005. Dependence of labradorite dissolution kinetics on CO_2 (aq), Al (aq), and temperature. Chem. Geol. 217 (3-4), 213-225.

Chandra, A.P., Gerson, A.R., 2010. The mechanisms of pyrite oxidation and leaching: A fundamental perspective. Surf. Sci. Rep. 65 (9), 293-315.

Charlton, T., Goodarzi, M., Rouainia, M., Aplin, A., Cubillas, P., 2021. Effect of diagenesis on geomechanical properties of organic-rich calcareous shale: A multiscale investigation. J. Geophys. Res.: Solid Earth 126 (7), e2020JB021365.

Chen, B., Xiang, J., Latham, J.-P., 2023. Influence of inter-grain cementation stiffness on the effective elastic properties of porous Bentheim sandstone. J. Rock Mech. Geotech. Eng. 15 (3), 573-583.

Chen, H., Hu, Y., Liu, J., Liu, F., Liu, Z., Kang, Y., Wang, X., 2021. Surface characteristics analysis of fractures induced by supercritical CO_2 and water through three-dimensional scanning and scanning electron micrography. J. Rock Mech. Geotech. Eng. 13 (5), 1047-1058.

Chen, Z., Bunger, A., Zhang, X., Jeffrey, R.G., 2009. Cohesive zone finite element-based modeling of hydraulic fractures. Acta Mech. Solida Sin. 22 (5), 443-452.

Chenevert, M., 1970. Shale control with balanced-activity oil-continuous muds. J. Pet. Technol. 22 (10), 1309-1316.

Cheng, Y., 2012. Impact of water dynamics in fractures on the performance of hydraulically fractured wells in gas-shale reservoirs. J. Can. Pet. Technol. 51 (02), 143-151.

Cheng, Y., Zeng, M., Lu, Z., Du, X., Yin, H., Yang, L., 2020. Effects of supercritical CO_2 treatment temperatures on mineral composition, pore structure and functional groups of shale: implications for CO_2 sequestration. Sustainability 12 (9), 3927.

Choobbasti, A.J., Kutanaei, S.S., 2017. Microstructure characteristics of cement-stabilized sandy soil using nanosilica. J. Rock Mech. Geotech. Eng. 9 (5), 981-988.

Chou, L., Garrels, R.M., Wollast, R., 1989. Comparative study of the kinetics and mechanisms of dissolution of carbonate minerals. Chem. Geol. 78 (3-4), 269-282.

Clarkson, C.R., Solano, N., Bustin, R.M., Bustin, A., Chalmers, G.R., He, L., Melnichenko, Y.B., Radliński, A., Blach, T.P., 2013. Pore structure characterization of North American shale gas reservoirs using USANS/SANS, gas adsorption, and mercury intrusion. Fuel 103, 606-616.

Colmenares, L.B., Zoback, M.D., 2002. A statistical evaluation of intact rock failure criteria constrained by polyaxial test data for five different rocks. Int. J. Rock Mech. Min. Sci. 39, 695-729.

Corapcioglu, H., Miskimins, J., Prasad, M. 2014. Fracturing fluid effects on Young's modulus and embedment in the Niobrara formation. In: SPE Annual Technical Conference and Exhibition. Society of Petroleum Engineers, Amsterdam, Netherlands.

Dai, J., Zou, C., Liao, S., Dong, D., Ni, Y., Huang, J., Wu, W., Gong, D., Huang, S., Hu, G., 2014. Geochemistry of the extremely high thermal maturity Longmaxi shale gas, southern Sichuan Basin. Org. Geochem. 74, 3-12.

Desbois, G., Urai, J., Kukla, P., 2009. Morphology of the pore space in claystones–evidence from BIB/FIB ion beam sectioning and cryo-SEM observations. eEarth Discussions 4 (1), 1-19.

Ding, W., Wang, H., Chen, H., Ma, T., 2021. Mechanical damage and chemical dissolution kinetic features of limestone under coupled mechanical-hydrological-chemical effects. Geofluids 2021, 1-8.

Dos Santos, E.C., de Mendonça Silva, J.C., Duarte, H.l.A., 2016. Pyrite oxidation mechanism by oxygen in aqueous medium. J. Phys. Chem. C 120 (5), 2760-2768.

Dozier, G., Elbel, J., Fielder, E., Hoover, R., Lemp, S., Reeves, S., Siebrits, E., Wisler, D., Wolhart, S., 2003. Refracturing works. Oilfield Review 15 (3), 38-53.

Du, J., Hu, L., Meegoda, J.N., Zhang, G., 2018. Shale softening: Observations, phenomenological behavior, and mechanisms. Appl. Clay Sci. 161, 290-300.

Du, J., Luo, S., Hu, L., Guo, B., Guo, D., Zhang, G., 2022. Multiscale mechanical properties of shales: grid nanoindentation and statistical analytics. Acta Geotech. 17 (2), 339-354.

Du, J., Whittle, A.J., Hu, L., Divoux, T., Meegoda, J.N., 2021. Characterization of meso-scale mechanical properties of Longmaxi shale using grid microindentation experiments. J. Rock Mech. Geotech. Eng. 13 (3), 555-567.

Du, J., Whittle, A.J., Hu, L., Divoux, T., Meegoda, J.N., 2023. Coupling grid nanoindentation and surface chemical analysis to infer the mechanical properties of shale mineral phases. Eng. Geol. 325, 107304.

Ebrahimi, D., Pellenq, R.J.M., Whittle, A.J., 2012. Nanoscale elastic properties of montmorillonite upon water adsorption. Langmuir 28 (49), 16855-16863.

Elia, P., Nativ-Roth, E., Zeiri, Y., Porat, Z.e., 2016. Determination of the average pore-size and total porosity in porous silicon layers by image processing of SEM micrographs. Microporous Mesoporous Mater. 225, 465-471.

Ellis, B.R., Fitts, J.P., Bromhal, G.S., McIntyre, D.L., Tappero, R., Peters, C.A., 2013. Dissolution-driven permeability reduction of a fractured carbonate caprock. Environ. Eng. Sci. 30 (4), 187-193.

Espinoza, D.N., Santamarina, J.C., 2012. Clay interaction with liquid and supercritical CO2: The relevance of electrical and capillary forces. Int. J. Greenhouse Gas Control 10, 351-362.

Feng, J., Tian, H., Huang, Y., Ding, Z., Yin, Z., 2019. Pyrite oxidation mechanism in aqueous medium. J. Chin. Chem. Soc. 66 (4), 345-354.

Feng, Y., Xiao, X., Gao, P., Wang, E., Hu, D., Liu, R., Li, G., Lu, C., 2023. Restoration of sedimentary environment and geochemical features of deep marine Longmaxi shale and its significance for shale gas: A case study of the Dingshan area in the Sichuan Basin, South China. Mar. Pet. Geol. 151, 106186.

Foster, W.R., Savins, J., Waite, J., 1955. Lattice expansion and rheological behavior relationships in water-montmorillonite systems. Clays Clay Miner. 395, 296-316.

Fuchs, S.J., Espinoza, D.N., Lopano, C.L., Akono, A.-T., Werth, C.J., 2019. Geochemical and geomechanical alteration of siliciclastic reservoir rock by supercritical CO_2-saturated brine formed during geological carbon sequestration. Int. J. Greenhouse Gas Control 88, 251-260.

Gao, Q., Tao, J., Hu, J., Yu, X.B., 2015. Laboratory study on the mechanical behaviors of an anisotropic shale rock. J. Rock Mech. Geotech. Eng. 7 (2), 213-219.

Gong, Q., Deng, J., Wang, Q., Yang, L., She, M., 2008. Calcite dissolution in deionized water from 50 °C to 250 °C at 10 MPa: rate equation and reaction order. Acta Geologica Sinica-English Edition 82 (5), 994-1001.

Goodarzi, M., Rouainia, M., Aplin, A., 2016. Numerical evaluation of mean-field homogenisation methods for predicting shale elastic response. Comput. Geosci. 20, 1109-1122.

Graham, S., Rouainia, M., Aplin, A., Ireland, M., Charlton, T., Armitage, P., 2022. New micromechanical data and modelling framework for the elastic response of calcareous mudstones. Int. J. Rock Mech. Min. Sci. 158, 105181.

Gundogar, A.S., Druhan, J., Ross, C.M., Jew, A.D., Bargar, J.R., Kovscek, A.R., 2022. Coreflood Effluent and Shale Surface Chemistries in Predicting Interaction between Shale, Brine, and Reactive Fluid. SPE J. 27 (04), 2283-2293.

Guo, H., He, M., Sun, C., Li, B., Zhang, F., 2012. Hydrophilic and strength-softening characteristics of calcareous shale in deep mines. J. Rock Mech. Geotech. Eng. 4 (4), 344-351.

Guo, X., Ni, H., Li, M., Zhang, L., Wang, Y., Ding, L., 2018. Experimental study on the influence of supercritical carbon dioxide soaking pressure on the mechanical properties of shale. Indian Geotechnical Journal 48, 384-391.

Gutjahr, A., Dabringhaus, H., Lacmann, R., 1996. Studies of the growth and dissolution kinetics of the $CaCO_3$ polymorphs calcite and aragonite I. Growth and dissolution rates in water. J. Cryst. Growth 158 (3), 296-309.

Han, Y., Kwak, D., Choi, S.Q., Shin, C., Lee, Y., Kim, H., 2017. Pore structure characterization of shale using gas physisorption: Effect of chemical compositions. Minerals 7 (5), 66.

He, J., Zhao, Z., Geng, Y., Chen, Y., Guo, J., Lu, C., Wang, S., Han, X., Zhang, J., 2023. Effect of fracture fluid flowback on shale microfractures using CT scanning. J. Rock Mech. Geotech. Eng. 16(2), 426-436.

He, M., Luis, S., Rita, S., Ana, G., Euripedes Jr, V., Zhang, N., 2011. Risk assessment of CO_2 injection processes and storage in carboniferous formations: a review. J. Rock Mech. Geotech. Eng. 3 (1), 39-56.

He, Z., Li, S., Nie, H., Yuan, Y., Wang, H., 2019. The shale gas “sweet window”:“The cracked and unbroken” state of shale and its depth range. Mar. Pet. Geol. 101, 334-342.

Holmes, P.R., Crundwell, F.K., 2000. The kinetics of the oxidation of pyrite by ferric ions and dissolved oxygen: an electrochemical study. Geochim. Cosmochim. Acta 64 (2), 263-274.

Huang, H., Li, R., Jiang, Z., Li, J., Chen, L., 2020. Investigation of variation in shale gas adsorption capacity with burial depth: Insights from the adsorption potential theory. J. Nat. Gas Sci. Eng. 73, 103043.

Jarvie, D.M., Hill, R.J., Ruble, T.E., Pollastro, R.M., 2007. Unconventional shale-gas systems: The Mississippian Barnett Shale of north-central Texas as one model for thermogenic shale-gas assessment. AAPG Bull. 91 (4), 475-499.

Jiang, X., Deng, S., Li, H., Zuo, H., 2022. Characterization of 3D pore nanostructure and stress-dependent permeability of organic-rich shales in northern Guizhou Depression, China. J. Rock Mech. Geotech. Eng. 14 (2), 407-422.

Ju, Y., Wang, G., Bu, H., Li, Q., Yan, Z., 2014. China organic-rich shale geologic features and special shale gas production issues. J. Rock Mech. Geotech. Eng. 6 (3), 196-207.

Kaestner, A., Lehmann, E., Stampanoni, M., 2008. Imaging and image processing in porous media research. Adv. Water Resour. 31 (9), 1174-1187.

Kang, Y., Shang, C., Zhou, H., Huang, Y., Zhao, Q., Deng, Z., Wang, H., Ma, Y.Z., 2020. Mineralogical brittleness index as a function of weighting brittle minerals—from laboratory tests to case study. J. Nat. Gas Sci. Eng. 77, 103278.

Katende, A. 2022. The Impact of Rock Lithology and Microstructural Properties on Proppant Embedment and Fracture Conductivity: A Case Study of the Caney Shale, Southern Oklahoma, USA, Oklahoma State University.

Katende, A., Allen, C., Massion, C., Awejori, A., Xiong, F., Radonjic, M., Rutqvist, J., Nakagawa, S. 2022. Experiments and modeling of proppant embedment and fracture conductivity for the Caney Shale, Oklahoma, USA. In: ARMA US Rock Mechanics/Geomechanics Symposium. ARMA, ARMA-2022-0805.

Katende, A., Awejori, G., Benge, M., Nakagawa, S., Wang, Y., Xiong, F., Puckette, J., Grammer, M., Rutqvist, J., Doughty, C. 2023a. Multidimensional, experimental and modeling evaluation of permeability evolution, the Caney Shale Field Lab, OK, USA. In: Unconventional Resources Technology Conference, 13–15 June 2023. Unconventional Resources Technology Conference (URTeC), 1505-1526.

Katende, A., Rutqvist, J., Benge, M., Seyedolali, A., Bunger, A., Puckette, J.O., Rhin, A., Radonjic, M., 2021. Convergence of micro-geochemistry and micro-geomechanics towards understanding proppant shale rock interaction: A Caney shale case study in southern Oklahoma, USA. J. Nat. Gas Sci. Eng. 96, 104296.

Katende, A., Rutqvist, J., Massion, C., Radonjic, M., 2023b. Experimental flow-through a single fracture with monolayer proppant at reservoir conditions: A case study on Caney Shale, Southwest Oklahoma, USA. Energy 273, 127181.

Khather, M., Saeedi, A., Myers, M.B., Giwelli, A., 2020. Effects of CO2-saturated brine on the injectivity and integrity of chalk reservoirs. Transp. Porous Media 135 (3), 735-751.

Kirstein, J., Hellevang, H., Haile, B.G., Gleixner, G., Gaupp, R., 2016. Experimental determination of natural carbonate rock dissolution rates with a focus on temperature dependency. Geomorphology 261, 30-40.

Kuang, L.-C., Hou, L.-H., Wu, S.-T., Cui, J.-W., Tian, H., Zhang, L.-J., Zhao, Z.-Y., Luo, X., Jiang, X.-H., 2022. Organic matter occurrence and pore-forming mechanisms in lacustrine shales in China. Pet. Sci. 19 (4), 1460-1472.

Lafollette, R.F., Carman, P.S. 2013. Comparison of the impact of fracturing fluid compositional ph on fracture wall properties in different shale formation samples. In: SPE Annual Technical Conference and Exhibition. Society of Petroleum Engineers. https://doi.org/10.2118/166471-MS.

Lahann, R., Mastalerz, M., Rupp, J.A., Drobniak, A., 2013. Influence of CO_2 on New Albany Shale composition and pore structure. Int. J. Coal Geol. 108, 2-9.

Lal, M. 1999. Shale stability: drilling fluid interaction and shale strength. In: *SPE Asia Pacific Oil and Gas Conference and Exhibition.* SPE, SPE-54356-MS.

Li, G., Jin, Z., Li, X., Zhang, P., Liang, X., Zhang, R., Li, C., Wang, D., Hu, Y., 2023a. Shallow burial shale gas accumulation pattern of the Wufeng–Longmaxi Formations in the northern Guizhou area, western Yangtze platform. Geoenergy Science and Engineering 225, 211683.

Li, Y., Peng, Y., Wei, Z., Yang, X., Gerson, A.R., 2023b. Crystal face-dependent pyrite oxidation: An electrochemical study. Appl. Surf. Sci. 619, 156687.

Liu, A., Liu, S., 2022. Mechanical property alterations across coal matrix due to water-CO_2 treatments: A micro-to-nano scale experimental study. Energy 248, 123575.

Liu, C.-D., Cheng, Y., Jiao, Y.-Y., Zhang, G.-H., Zhang, W.-S., Ou, G.-Z., Tan, F., 2021. Experimental study on the effect of water on mechanical properties of swelling mudstone. Eng. Geol. 295, 106448.

Liu, J., Ma, S., Ni, H., Pu, H., Li, X., Chen, S., 2022. Quantitative two/three-dimensional spatial characterization and fluid transport prediction of macro/micropores in Gaomiaozi bentonite. J. Rock Mech. Geotech. Eng. 14 (5), 1568-1579.

Liu, K., Jin, Z., Zeng, L., Ozotta, O., Gentzis, T., Ostadhassan, M., 2023. Alteration in the mechanical properties of the Bakken during exposure to supercritical CO_2. Energy 262, 125545.

Liu, Q., Lu, Y., Zhang, F.e., 2013. Laboratory simulation experiment on dissolution of limestone under hydrodynamic pressure. Carbonates Evaporites 28, 3-11.

Lu, Y., Ao, X., Tang, J., Jia, Y., Zhang, X., Chen, Y., 2016. Swelling of shale in supercritical carbon dioxide. J. Nat. Gas Sci. Eng. 30, 268-275.

Luo, S., Kim, D., Wu, Y., Li, Y., Wang, D., Song, J., DeGroot, D.J., Zhang, G., 2021. Big data nanoindentation and analytics reveal the multi-staged, progressively-homogenized, depth-dependent upscaling of rocks' properties. Rock Mech. Rock Eng. 54, 1501-1532..

Luo, S., Lu, Y., Wu, Y., Song, J., DeGroot, D.J., Jin, Y., Zhang, G., 2020. Cross-scale characterization of the elasticity of shales: Statistical nanoindentation and data analytics. J. Mech. Phys. Solids 140, 103945.

Lutz, J.F., 1935. THE RELATION OF SOIL EROSION TO CERTAIN INHERENT SOIL PROPERTIES. Soil Sci. 40 (6), 439-458.

Ma, T., Chen, P., 2014. Study of meso-damage characteristics of shale hydration based on CT scanning technology. Pet. Explor. Dev. 41, 249-256.

Manjunath, G., Akono, A.-T., Haljasmaa, I., Jha, B., 2023. Role of CO_2 in geomechanical alteration of Morrow Sandstone across micro–meso scales. Int. J. Rock Mech. Min. Sci. 163, 105311.

Mathia, E.J., Rexer, T.F., Thomas, K.M., Bowen, L., Aplin, A.C., 2019. Influence of clay, calcareous microfossils, and organic matter on the nature and diagenetic evolution of pore systems in mudstones. J. Geophys. Res.: Solid Earth 124 (1), 149-174.

Medina-Rodriguez, B.X., Frouté, L., Alvarado, V., Kovscek, A.R., 2023. Multimodal study of the impact of stimulation pH on shale pore structure, with an emphasis on organics behavior in alkaline environments. Fuel 331, 125649.

Meng, J., Chen, S., Wang, J., Chen, Z., Zhang, J., 2022. Development and application of carbonate dissolution test equipment under thermal–hydraulic–chemical coupling condition. Materials 15 (20), 7383.

Mody, F.K., Hale, A.H., 1993. Borehole-stability model to couple the mechanics and chemistry of drilling-fluid/shale interactions. J. Pet. Technol. 45 (11), 1093-1101.

Nguyen, B.N., Hou, Z., Last, G.V., Bacon, D.H., 2016. Three-dimensional analysis of a faulted CO_2 reservoir using an Eshelby-Mori-Tanaka approach to rock elastic properties and fault permeability. J. Rock Mech. Geotech. Eng. 8 (6), 828-845.

Norrish, K., 1954. The swelling of montmorillonite. Discuss. Faraday Soc. 18, 120-134.

O'Brien, D.E., Chenevert, M.E., 1973. Stabilizing sensitive shales with inhibited, potassium-based drilling fluids. J. Pet. Technol. 25 (9), 1089-1100.

Oliver, W.C., Pharr, G.M., 1992. An improved technique for determining hardness and elastic modulus using load and displacement sensing indentation experiments. J. Mater. Res. 7, 1564.

Oliver, W.C., Pharr, G.M., 2004. Measurement of hardness and elastic modulus by instrumented indentation: Advances in understanding and refinements to methodology. J. Mater. Res. 19, 3-20.

Ortega, J.A., Ulm, F.J., Abousleiman, Y., 2007. The effect of the nanogranular nature of shale on their poroelastic behavior. Acta Geotech. 2, 155-182.

Pan, L., Xiao, X., Tian, H., Zhou, Q., Cheng, P., 2016. Geological models of gas in place of the Longmaxi shale in Southeast Chongqing, South China. Mar. Pet. Geol. 73, 433-444.

Pan, X., Guo, W., Wu, S., Chu, J., 2020. An experimental approach for determination of the Weibull homogeneity index of rock or rock-like materials. Acta Geotech. 15, 375-391.

Pan, Z., Connell, L.D., 2007. A theoretical model for gas adsorption-induced coal swelling. Int. J. Coal Geol. 69 (4), 243-252.

Peirce, A.P., Bunger, A.P., 2015. Interference fracturing: nonuniform distributions of perforation clusters that promote simultaneous growth of multiple hydraulic fractures. SPE J. 20 (02), 384-395.

Pimienta, L., Esteban, L., Sarout, J., Liu, K., Dautriat, J., Delle Piane, C., Clennell, M.B., 2017. Supercritical CO_2 injection and residence time in fluid-saturated rocks: Evidence for calcite dissolution and effects on rock integrity. Int. J. Greenhouse Gas Control 67, 31-48.

Plummer, L.N., Wigley, T.M., Parkhurst, D.L., 1978. The kinetics of calcite dissolution in CO_2-water systems at 5 degrees to 60 degrees C and 0.0 to 1.0 atm CO_2. Am. J. Sci. 278 (2), 179-216.

Qin, J., Pang, X., Santra, A., Cheng, G., Li, H., 2023. Various admixtures to mitigate the long-term strength retrogression of Portland cement cured under high pressure and high temperature conditions. J. Rock Mech. Geotech. Eng. 15 (1), 191-203.

Ren, Z., Zhang, S., Gao, S., Cui, J., Xiao, Y., Xiao, H., 2007. Tectonic thermal history and its significance on the formation of oil and gas accumulation and mineral deposit in Ordos Basin. Science in China Series D: Earth Sciences 50, 27-38.

Rickman, R., Mullen, M.J., Petre, J.E., Grieser, W.V., Kundert, D. 2008. A practical use of shale petrophysics for stimulation design optimization: all shale plays are not clones of the Barnett Shale. In: SPE Annual Technical Conference and Exhibition. Society of Petroleum Engineers, Denver, Colorado, USA.

Shah, M., Shah, S., Sircar, A., 2017. A comprehensive overview on recent developments in refracturing technique for shale gas reservoirs. J. Nat. Gas Sci. Eng. 46, 350-364.

Simpson, G.J., Sedin, D.L., Rowlen, K.L., 1999. Surface roughness by contact versus tapping mode atomic force microscopy. Langmuir 15, 1429-1434.

Sjoberg, E., 1978. Kinetics and mechanism of calcite dissolution in aqueous solutions at low temperature temperatures. Stockholm Contrib. Geol. 32, 1-92.

Sjöberg, E.L., Rickard, D.T., 1984. Temperature dependence of calcite dissolution kinetics between 1 and 62 °C at pH 2.7 to 8.4 in aqueous solutions. Geochim. Cosmochim. Acta 48 (3), 485-493.

Sposito, G. 1989. The chemistry of soils. Oxford Univ, New York, USA.

Sreekanth, M., Bambole, V., Mhaske, S., Mahanwar, P., 2009. Effect of concentration of mica on properties of polyester thermoplastic elastomer composites. Journal of Minerals & Materials Characterization & Engineering 8 (4), 271-282.

Sun, X., Wang, J., Wang, H., Miao, L., Cao, Z., Wu, L., 2024. Bio-cementation for tidal erosion resistance improvement of foreshore slopes based on microbially induced magnesium and calcium precipitation. J. Rock Mech. Geotech. Eng. 16 (5), 1696-1708.

Sun, Y., Li, Q., Yang, D., Liu, X., 2016. Laboratory core flooding experimental systems for CO_2 geosequestration: An updated review over the past decade. J. Rock Mech. Geotech. Eng. 8 (1), 113-126.

Taghichian, A., Hashemalhoseini, H., Zaman, M., Zavareh, S.B., 2018. Propagation and aperture of staged hydraulic fractures in unconventional resources in toughness-dominated regimes. J. Rock Mech. Geotech. Eng. 10 (2), 249-258.

Tang, Q., Gratchev, I., 2023. Estimation of sedimentary rock porosity using a digital image analysis. Applied Sciences 13 (4), 2066.

Vandamme, M., Brochard, L., Lecampion, B., Coussy, O., 2010. Adsorption and strain: the CO_2-induced swelling of coal. J. Mech. Phys. Solids 58 (10), 1489-1505.

Wang, D., Li, S., Wang, R., Li, B., Pan, Z., 2024. Evaluating the stability and volumetric flowback rate of proppant packs in hydraulic fractures using the lattice Boltzmann-discrete element coupling method. J. Rock Mech. Geotech. Eng. 16 (6), 2052-2063.

Wang, J., Ju, Y., Gao, F., Liu, J., 2016. A simple approach for the estimation of CO_2 penetration depth into a caprock layer. J. Rock Mech. Geotech. Eng. 8 (1), 75-86.

Wang, J., Rahman, S.S. 2015. An investigation of fluid leak-off due to osmotic and capillary effects and its impact on micro-fracture generation during hydraulic fracturing stimulation of gas shale. In: EUROPEC 2015. Society of Petroleum Engineers, Madrid, Spain.

Wang, Y., Dong, D., Li, J., Wang, S., Li, X., Wang, L., Cheng, K., Huang, J., 2012. Reservoir characteristics of shale gas in Longmaxi Formation of the Lower Silurian, southern Sichuan. Shiyou Xuebao/Acta Petrolei Sinica 33, 551-561.

Wang, Y., Luo, G., Achang, M., Cains, J., Wethington, C., Katende, A., Grammer, G.M., Puckette, J., Pashin, J., Castagna, M., 2021. Multiscale characterization of the caney shale—an emerging play in Oklahoma. Midcontinent Geoscience 2, 33-53.

Wong, R., 1998. Swelling and softening behaviour of La Biche shale. Can. Geotech. J. 35 (2), 206-221.

Wu, H., Hu, L., Wen, Q., 2015a. Electro-osmotic enhancement of bentonite with reactive and inert electrodes. Appl. Clay Sci. 111, 76-82.

Wu, H., Hu, L., Zhang, L., Wen, Q., 2015b. Transport and exchange behavior of ions in bentonite during electro-osmotic consolidation. Clays Clay Miner. 63 (5), 395-403.

Yang, Y., Liu, S., 2020. Review of shale gas sorption and its models. Energy Fuels 34 (12), 15502-15524.

Yin, H., Zhou, J., Xian, X., Jiang, Y., Lu, Z., Tan, J., Liu, G., 2017. Experimental study of the effects of sub-and super-critical CO_2 saturation on the mechanical characteristics of organic-rich shales. Energy 132, 84-95.

Yin, Z., Huang, H., Zhang, F., Zhang, L., Maxwell, S., 2020. Three-dimensional distinct element modeling of fault reactivation and induced seismicity due to hydraulic fracturing injection and backflow. J. Rock Mech. Geotech. Eng. 12 (4), 752-767.

Yu, H., Lu, C., Chen, W., Yang, D., Li, H., 2022. Characterization of microstructural features of Tamusu mudstone. J. Rock Mech. Geotech. Eng. 14 (6), 1923-1932.

Zeppenfeld, K., 2010. Prevention of $CaCO_3$ scale formation by trace amounts of copper (II) in comparison to zinc (II). Desalination 252 (1-3), 60-65.

Zhang, D., Ranjith, P., Perera, M., 2016. The brittleness indices used in rock mechanics and their application in shale hydraulic fracturing: A review. Journal of petroleum science and Engineering 143, 158-170.

Zhang, G., Wei, Z., Ferrell, R.E., Guggenheim, S., Cygan, R.T., Luo, J., 2010. Evaluation of the elasticity normal to the basal plane of non-expandable 2:1 phyllosilicate minerals by nanoindentation. Am. Mineral. 95, 863-869.

Zhang, J., Kamenov, A., Zhu, D., Hill, A. 2013. Laboratory measurement of hydraulic fracture conductivities in the Barnett shale. In: IPTC 2013: International Petroleum Technology Conference, Beijing, China.

Zhang, P., Celia, M.A., Bandilla, K.W., Hu, L., Meegoda, J.N., 2020. A Pore-network simulation model of dynamic CO_2 migration in organic-rich shale formations. Transp. Porous Media 133 (3), 479-496.

Zhang, Y., Long, A., Zhao, Y., Zang, A., Wang, C., 2023. Mutual impact of true triaxial stress, borehole orientation and bedding inclination on laboratory hydraulic fracturing of Lushan shale. J. Rock Mech. Geotech. Eng. 15 (12), 3131-3147.

Zhang, Z., Low, P., 1989. Relation between the heat of immersion and the initial water content of Li-, Na-, and K-montmorillonite. J. Colloid Interface Sci. 133 (2), 461-472.

Jianting Du received his PhD in Civil Engineering from Tsinghua University, Beijing, China in 2020, and worked as a Post-Doctoral Fellow at University of Hong Kong from 2020 to 2022. He is currently a research assistant professor at University of Macau, China. His research interests include (1) the multiscale characterization of composite materials (e.g. rocks), (2) shale softening behavior and mechanisms, and (3) geo-storage of carbon dioxide.

Highlights:

a) Mechanical alterations induced by shale-fluids interactions are evaluated at mesoscale.
b) Underlying mechanisms are revealed by in-situ morphological and mineralogical identification.
c) Carbonate dissolution, clay swelling, and pyrite oxidation are dominant mechanisms.

Declaration of interests

☒ The authors declare that they have no known competing financial interests or personal relationships that could have appeared to influence the work reported in this paper.

☐The authors declare the following financial interests/personal relationships which may be considered as potential competing interests: